Uplink Secure Receive Spatial Modulation Empowered by Intelligent Reflecting Surface

Chaowen Liu, *Member, IEEE,* Zhengmin Shi, *Graduate Student Member, IEEE,* Menghan Lin, *Graduate Student Member, IEEE,* Fei Yu, *Graduate Student Member, IEEE,* Tong-Xing Zheng, *Member, IEEE,* Jiankang Zhang, *Senior Member, IEEE,* and Guangyue Lu, *Member, IEEE*

***Abstract*—With the emergence of the fifth generation (5G) era, the development of the Internet of Things (IoT) network has been accelerated with a new impetus, making it imperative to strive for a more reliable and efficient network environment. To accomplish this, we introduce and investigate a novel proposal for the intelligent reflecting surface (IRS) enabled uplink secure receive spatial modulation (SM), named IRS-USRSM, to resolve the security issues arising from the open wireless transmission environment in the 5G IoT network. In the IRS-USRSM scheme, we assume that the passive eavesdropper is directly connected to the uplink user and occasionally connected to the IRS. To achieve enhanced secrecy with finite alphabet inputs, a joint transmitter perturbation and IRS reflection design for physical layer security is proposed to guarantee secure and reliable transmission of IRS-USRSM. Specifically, two categories of IRS-based random phase compensation strategies, namely, random perturbation compensation and random path synthesize, along with maximum likelihood detection and suboptimal detection are proposed to meet the variant design requirements between achieved performance and system cost. Furthermore, in order to evaluate the performance limits of the IRS-USRSM, the closed-form results of average bit error probabilities and discrete-input continuous-output memoryless channel capacities are derived using the method of moment generating function. Simulation results are presented to verify the correctness of our theoretical analyses, as well as to demonstrate the efficiency and superiority of the proposed IRS-USRSM scheme.**

***Index Terms*—Intelligent reflecting surface; secure receive spatial modulation; finite alphabet inputs; physical layer security; performance evaluation.**

This work was supported in part by the National Natural Science Foundation of China under Grant 61901366, in part by the Key Research and Development Project of Shaanxi Province under Grant 2023-YBGY-272. The work of Tong-Xing Zheng was supported in part by the Aeronautical Science Foundation of China under Grant ASFC-2022Z021070001, in part by the China Postdoctoral Science Foundation under Grants 2021M702631. The work of Guangyue Lu was supported in part by the National Natural Science Foundation of China under Grant 62201451 and 62271368, in part by the Key Research and Development Project of Shaanxi under Grant 2023-YBGY-041, in part by the Fundamental Research Funds for the Central Universities. Part of the paper has been presented at the IEEE VTC2023-Fall [1]. *(Corresponding authors: Jiankang Zhang and Guangyue Lu.)*

Chaowen Liu, Zhengmin Shi, Fei Yu and Guangyue Lu are with the School of Telecommunication and Information Engineering, Xi'an University of Posts and Telecommunications, Xi'an 710121, P. R. China. (e-mail: liucw@xupt.edu.cn; shizhengmin@stu.xupt.edu.cn; yf@stu.xupt.edu.cn; tonylugy@163.com).

Menghan Lin and Tong-Xing Zheng are with the School of Information and Communications Engineering, Xi'an Jiaotong University, Xi'an 710049, China (e-mail: linmh0130@stu.xjtu.edu.cn; zhengtx@mail.xjtu.edu.cn).

Jiankang Zhang is with the Department of Computing and Informatics, Bournemouth University, BH12 5BB Bournemouth, U.K. (e-mail: jzhang3@bournemouth.ac.uk).

I. Introduction

A. Background & Related Works

Incorporated with the fifth generation (5G) mobile communication technologies, the Internet of Things (IoT) network has rapidly advanced as a promising paradigm for revolutionizing various industries and domains, including transportation, energy, and agriculture, among others [2]. Effective deployment of IoT networks relies heavily on the seamless integration of various wireless communication technologies such as Wi-Fi, Bluetooth, and ZigBee [3]. In face of these, it is imperative for us to address two key issues of efficient and secure transmission, so as to facilitate the network-wide connection and operation of ubiquitous terminals, which are employed with different communication mechanisms [4], [5].

Against the background of beyond 5G, intelligent reflecting surface (IRS) has emerged as a key enabling technology, which is capable of unlocking new avenues in the research field of diverisity-augmented wireless [6]. In practical scenarios, communication links frequently confront multipath and blocking effects caused by obstacles, which deteriorate the transmission performance heavily. To deal with this, one can resort to the conventionally utilized relay or the recently promising IRS engaged solution. However, the relay system requires additional energy to process and retransmit the signals [7], which may cause infeasibility in assisting resources-constrained transmissions. Fortunately, the IRS is proved to be able to assist quality and efficiency enhanced transmissions without extra energy consumption [8]–[11]. In [12], the authors have proposed to utilize IRS-assisted satellite transmission, such that the achievable downlink and uplink transmission rates can be significantly enhanced for the engaged IoT networks. Moreover, in [13], the authors have introduced and investigated the IRS-assisted downlink non-orthogonal multiple access (NOMA) IoT networks, where the NOMA-based clustering schemes are exploited to achieve remarkably improved throughput and reliability. Albeit with these merits, the secrecy of the openness transmissions between resources-constrained network nodes remain to be resolved.

By activating a single antenna to transmit additional information, spatial modulation (SM) is proposed as a novel multiple-input multiple-output (MIMO) technology that can be employed to assist wireless transmissions with elevated spectral and energy efficiency [14]–[17]. Based on the channel-adapted control of transmission signals, IRS-assisted SM can be utilized to provide the modulated wireless MIMO with

further enhanced reliability and efficiency [18]–[20]. For instance, by merging the philosophy of IRS with that of SM, the authors of [21] have proposed the IRS-assisted receive quadrature SM (IRS-QSM) scheme to improve the reliability of wireless transmissions. In addition, the authors of [22] have proposed to implement the IRS-QSM at both-ends of the transmitter and receiver, such that the spectral efficiency and reliability of the wireless MIMOs can be further boosted. Whereas, while SM and IRS can bring wireless systems with considerable performance augment, it still cannot guarantee the transmission security by only itself.

With the fast growth of sensitive and confidential information transmissions, the significance of addressing the involved secrecy issues becomes more pronounced [23]. Unlike conventional encryption strategies, the physical layer security (PLS) category schemes bolster security by harnessing the natural unpredictability of the communication channels [24]–[26]. To be specific, the PLS guaranteeing proposal is often exposed with secure transmission solutions of secrecy beamforming, cooperative relaying and constructive interference utilizing [27]–[29]. For instance, in [30], the authors have proposed an artificial noise assisted quaternary virtual channel spatial modulation for guaranteeing the secrecy of a dual-hop communication system. By regulating the on/off states of IRS elements, the authors of [31] have proposed and studied a secure SM with passive beamforming and information transmission simultaneously executed at the IRS. Further, the authors of [32] have proposed to combine a novel multi-antenna transmitter precoding scheme with receive spatial modulation, so as to prevent multi-user NOMA MIMO visible light communication from being intercepted by a passive eavesdropper. Apart from the superiorities in secrecy performance enhancing, the above-mentioned PLS ensuring schemes are implemented with additional request of antenna resources and system overheads for facilitating transmitter AN injection, secure precoding and interception beam-fouling. Similarly, in the related research works [33]–[35], the artificial noise, beamforming, and precoding schemes are introduced for achieving secure transmission with IRS. However, these proposals are mainly implemented with additional request of transmission resources. This as a result, impede the existing schemes from being suitably applied in the IoT transmissions with limited resource budget.

B. Motivations & Contributions

Despite the extensive research on frameworks based on IRS, SM, and/or PLS, most current studies primarily focus on the reliability or security of the system, without a detailed analysis of both perspectives within the same model. Besides, to the best of our knowledge, there exists no research works that consider to put-forward reliable and secure transmission for IRS-assisted uplink wireless with restricted single-antenna involved transmitting resources. In light of these, a novel scheme named IRS-assisted uplink secure receive spatial modulation (USRSM) is and investigated. Specifically, we consider the uplink wiretapping system with a multi-antenna eavesdropper, where a user with a single antenna transmits signals containing both confidential information and multiplicative perturbation to a multi-antenna basestation modulated with receive spatial modulation. Based on this conceptual framework, this paper will conduct specific performance evaluations for both the basestation and eavesdropping end under different transmission schemes and eavesdropping scenarios, so as to verify the feasibility and effectiveness of our novel proposal.

To elaborate further, the main contributions of this paper are summarized as follows:

- A novel proposal of IRS empowered USRSM (IRS-USRSM) is introduced and investigated. By which, the secrecy of the single-input multiple-output (SIMO) systems with finite-alphabet inputs can be guaranteed by injecting symbol-rate associated random perturbations at the user-end in a comprehensive manner. Further, we address with both the worst and ideal eavesdropping scenarios based on whether the IRS has a direct link to the passive eavesdropper or not, so as to substantiate the efficiency in PLS protection of our proposal.
- We introduce novel IRS-assisted transmission and receiver detection schemes, such that the efficiency and reliability performance of the IRS-USRSM can be guaranteed, while different tradeoffs between system performance and implementation cost can be achieved. Specifically, we propose and investigate both IRS element and group-wise random path synthesization (RPS) and random perturbation compensation (RPC) based joint transmitter perturbation and IRS reflection (JTPIR) schemes. On the other hand, for receive signal detecting, the maximum likelihood detection (MLD) and suboptimal detection are raised for implementing with different levels of computational complexity.
- Closed-form secrecy performance of the IRS-USRSM are evaluating by determinating the discrepancies between the average bit error rate (ABEP) and discrete-input continuous-output memoryless channel capacity (DCMCC) performance achieved by the basestation and eavesdropper, respectively. Specifically, we derive the best reliability and secrecy performance of the IRS-USRSM, which is achieved with element-wise RPC based JTPIR and MLD. The closed-form ABEP and DCMCC performance results are deduced by utilizing the moment generating function (MGF), central limit theorem (CLT), and the gamma approximation methods.

C. Organization & Notations

The rest of the paper is organized as follows. In Section II, we briefly introduce the traditional RSM system and the proposed USRSM system. Section III presents two transmission schemes, RPS and RPC, as well as two phase alignment schemes. In Section IV, we describe the MLD algorithm and the suboptimal detection algorithm. In Section V, we analyze the BER and achieved ergodic secrecy rate (ESR). The simulation results are presented in Section VI, with the conclusions presented in Section VII and the appendix in Section VIII.

Notations: Lowercase and uppercase bold letters represent vectors and matrices, respectively. $(\cdot)^T$, $(\cdot)^H$, and $(\cdot)^*$ denote

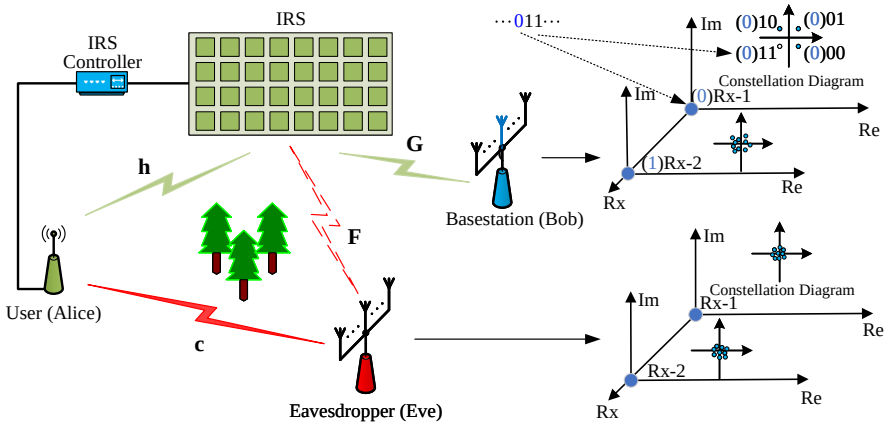

Fig. 1. An illustration of the proposed IRS-USRSM system.

the transposition, Hermitian transposition, and complex conjugation of a vector/matrix respectively. $\mathrm{diag}(\mathbf{A})$ represents the diagonal matrix of $\mathbf{A}$. $\det(\cdot)$ stands for the matrix determinant. $||\cdot||$ denotes the 2-norm of a vector. $\Re\{\cdot\}$ denotes the real part. $\mathbb{E}[\cdot]$ and $\mathbb{D}[\cdot]$ denote the mean and variance of a random variable respectively. $\mathcal{CN}(\mu,\sigma^2)$ stands for complex Gaussian distribution with mean μ and variance σ^2. $\mathcal{H}(\cdot)$ and $\mathcal{H}(\cdot|\cdot)$ represent the marginal and conditional entropy, respectively. $\Gamma(\varepsilon,\beta)$ represents Gamma function with the shape parameter ε and the scale parameter β.

II. System Proposal and Modelling

In this section, we begin with a brief retrospection of the conventional benchmark IRS-assisted receive spatial modulation (IRS-RSM). After that, a novel IRS-USRSM system that takes into account the security of wireless transmission is proposed, where a multiplicative random perturbation is injected at the transmitter in an on-the-fly manner. By doing so, the information recovering quality is enhanced at the basestation, while remains undetermined at the eavesdropper. To make sure the paper is self-contained, this section briefly reviews the conventional IRS-RSM system and then describe in detail the proposed IRS-USRSM system, both of which are transmitted with the assist of N elements of IRS.

A. Conventional IRS-RSM

For the traditional IRS-RSM proposed in [36], the base-band and spatial bits separately for each transmission duration. Specifically, the base-band bits are mapped and modulated to an M-ary amplitude-phase modulation (APM) symbol, while the spatial bits to one of the indices of N_b antennas at Bob. To this end, the number of bits transmitted per channel use (bpcu) can be formulated as

$$b = \log_2(M) + \log_2(N_b). \tag{1}$$

Let the diagonal reflection coefficient matrix of the IRS be $\mathbf{\Phi}$=diag($\boldsymbol{\varphi}$), while the reflection coefficient vector be $\boldsymbol{\varphi}$=$[e^{-j\varphi_1}, e^{-j\varphi_2}, ..., e^{-j\varphi_l}, ..., e^{-j\varphi_N}]$. Here φ_l is the phase shift of the l-th IRS reflecting element, which is selected from $[0, 2\pi)$. The channel matrix of the Alice-to-IRS and IRS-to-Bob links are respectively denoted as $\mathbf{h} = [h_1, h_2, ..., h_N]^T \in \mathbb{C}^{N\times 1}$ and $\mathbf{G} = [\mathbf{g}_1, \mathbf{g}_2, ..., \mathbf{g}_l, ..., \mathbf{g}_N] \in \mathbb{C}^{N_b\times N}$, where $\mathbf{g}_l \in \mathbb{C}^{N_b\times 1}$ is the channel vector from the l-th IRS element to Bob. Then, the received signal at Bob can be given by

$$\mathbf{y} = \mathbf{G}\mathbf{\Phi}\mathbf{h}x_k + \mathbf{n}, \tag{2}$$

where x_k represents the k-th APM symbol with $\mathbb{E}[|x_k|^2] = 1$.

Note that, due to the lack of security-guaranteeing countermeasures, the signal observed by the passive eavesdropper holds essentially the same form as that of the IRS-RSM receiver Bob. Hence, the detection can be ideally conducted at Eve at least for recovering the baseband portion of bits, which poses a substantial threat to the information secrecy of legitimate communicating parties. To cope with this, we propose and detail the IRS-USRSM, which is capable of achieving remarkably enhanced transmission security without extra power and hardware consumption.

B. Proposed IRS-USRSM

In Fig.1, the IRS-USRSM is proposed for assisting the secure transmission of uplink wiretap system which consists of a single antenna user (Alice), a N_b antenna basestation (Bob), an IRS with N reflecting elements, and a N_e antenna passive eavesdropper (Eve) linked directly with Alice. Here, N is a non-negative integer power of 2. The involved channels are assumed to satisfy Rayleigh fading $\mathcal{CN}(0,\sigma^2)$. For ease of understanding, the channel state informations (CSIs) are assumed to be ideally obtained by the legitimate transceivers. The M-ary APM symbols are transmitted with the injection of multiplicative random perturbations, while the spatial symbols are embedded with the indices of antennas at Bob upon employing the perturbation compensation oriented IRS reflection strategies. Then, due to the distinct fading of wireless channels, the quality of received signal at unauthorized antennas/terminals, including Eve, can be deteriorated heavily, which indicates a higher level of security against undetermined eavesdropping.

1) System Model: As shown in Fig. 1, in the IRS-USRSM system, the single-antenna Alice transmits signals with confidential information to Bob in the presence of passive Eve through the assistance of IRS, where the reflection phases of the IRS and the channel setups are similar to the conventional

IRS-RSM. As discussed in many works, we explicitly adopt that direct connection between Alice and Bob is not available due to obstacles. The IRS controller is responsible for adjusting the reflection phases and amplitudes of the IRS element. To avoid the performance loss caused by the scaled signals, the amplitudes of the IRS element are set to equal a maximum value of 1. In this paper, we assume that the distance between horizontally and vertically adjacent IRS elements is larger than half of the carrier wavelength, while ignore signals reflected two or more times by IRS due to severe path loss.

Let us denote the direct channel between Alice and Eve as $\mathbf{c} \in \mathbb{C}^{N_e \times 1}$, while the channel between IRS and Eve as $\mathbf{F} \in \mathbb{C}^{N_e \times N}$. For the benefit of discussing the limits of security performance, we assume that Eve has access to the CSI of each link from Alice to Eve[1]. However, due to the uncertainty of Eve's position, the connection channels may occasionally be blocked. Accordingly, we consider and investigate two eavesdropping scenarios: 1) the first is the ideal eavesdropping scenario, namely Scenario $\mathcal{I}$, wherein the direct eavesdropping link denoted by $\mathbf{c}$ retains, while the reflecting link denoted by $\mathbf{F}$ is effectively blocked. 2) the second is the worst eavesdropping scenario, namely Scenario $\mathcal{J}$, where both links denoted by $\mathbf{c}$ and $\mathbf{F}$ exist.

Notice that, although more realistic transmission scenarios are considered, the achieved data rate of the IRS-USRSM is the same as that of the conventional IRS-RSM. As shown in Fig. 1, given that the data-bit segment of '011' is delivered in the current time-slot, the first bit is guided to activate the first receiving antenna (i.e., Rx-1) at Bob, while the subsequent two bits are mapped and modulated to an M-ary APM symbol.

2) Signal Model: In the proposed IRS-USRSM, Alice transmits perturbed confidential M-ary APM symbol of S_k to Bob via IRS, which can be written as

$$S_k = e^{-jQ} x_k, \tag{3}$$

where, Q is the phase opposite of the normalized multiplicative perturbation factor e^{-jQ}. Given arbitrarily experienced eavesdropping, the received signal at Bob can be modeled as

$$\mathbf{y}_b = \mathbf{G}\Phi\mathbf{h}S_k + \mathbf{n}_b, \tag{4}$$

where $\mathbf{n}_b = [n_{b1}, n_{b2}, ..., n_{bN_b}]^T$ is the noise vector at Bob with entries following the distribution of $\mathcal{CN}(0, \sigma_b^2)$.

For individual scenarios of $\mathcal{I}$ and $\mathcal{J}$, the observed signals at Eve can be represented respectively as

$$\mathbf{y}_e^{\mathcal{I}} = \mathbf{c}S_k + \mathbf{n}_e, \tag{5}$$

$$\mathbf{y}_e^{\mathcal{J}} = (\mathbf{c} + \mathbf{F}\mathbf{\Phi}\mathbf{h})S_k + \mathbf{n}_e, \tag{6}$$

where $\mathbf{n}_e = [n_{e1}, n_{e2}, ..., n_{eN_e}]^T$ represents the noise vector at Eve with each of its elements satisfying the distribution of $\mathcal{CN}(0, \sigma_e^2)$. Details of JTPIR based secure transmission strategies for accomplishing the IRS-USRSM will be presented in the following section.

[1]In this paper, we assume that Bob and Eve are capable of attaining respectively the CSI of the equivalent cascaded legitimate link, and that of the direct/cascaded link upon employing the common pilot signal, so as to validate the reasonableness and superior effectiveness of the IRS-USRSM proposal.

III. Joint Transmitter Perturbation and IRS Reflection Design

In this section, we present two JTPIR designs, which are based on the RPS and RPC for realizing different system cost and secrecy performance trade-offs. Given the mentioned designs are utilized, the uplink user Alice randomly selects the multiplicative perturbation, or dedicatedly designs the multiplicative perturbation via employing the available perfect CSI. In order to achieve enhanced secrecy with different levels of complexities of IRS and IRS controller, we introduce the proposals of element-wise and group-wise RPS/RPC (ERPS/ERPC and GRPS/GRPC). With the ERPS/ERPC, each IRS element is engaged with individual reflecting coefficient independently. By contrast, for the GRPS/GRPC, the IRS elements within the same group are configured with the same reflecting coefficient. Owing to the employment of JTPIR, the constellation points collect by the activated receiving antenna of Bob are observed as a regular pattern, while those collected by the arbitrary antenna of Eve are randomly scrambled. Below, we elaborate with more details.

A. JTPIR Design Based on RPS

In principle, for the RPS based JTPIR, the phases of IRS reflecting coefficients are randomly designated. Then, for the uplink user Alice, the multiplicative perturbation is dedicatedly designed and injected, such that the phase distortion yielded upon the synthesizing of equivalent random legitimate channel paths is appropriately compensated, while that by the synthesizing of equivalent random illegitimate channel paths remains rapidly perturbed. Accordingly, Bob is predicted to be able to achieve regular APM constellations observation at the activated antenna without additional operations. By contrast, Eve is foreseen to be not capable of observing regular symbol constellation at any of its antennas, and is hence unable to correctly recover the confidential information bit. For better understanding, the RPS is categorised into the ERPS and GRPS while the details of ERPS/GRPS are respectively elaborated as follows.

1) ERPS Based Design: Upon recalling (4), the signal observed by the i-th antenna of Bob with the ERPS is

$$y_{bi}^{ES} = \sum_{l=1}^{N} g_{il} h_l e^{-j\varphi_l} S_k^{ES} + n_{bi}, \tag{7}$$

where h_l represents the channel gain from Alice to the l-th element of IRS, g_{il} is the channel gain from the l-th element of the IRS to the i-th 'activated' receiving antenna at Bob, i.e., the i-th row element of the vector $\mathbf{g}_l$, and $\varphi_l \in (0, 2\pi]$ is the phase shift of the l-th reflecting element of IRS.

To ensure that signal part of y_{bi}^{ES} is regularly synthesized with equivalent vector paths, we formulate and design S_k^{ES} as

$$S_k^{ES} = e^{-jQ_i^{ES}} x_k, \tag{8}$$

where Q_i^{ES} denotes the phase of the multiplicative perturbation factor based on ERPS when the i-th receive antenna is activated. Then, Q_i^{ES} can be obtained by applying the scheme of ERPS as

$$Q_i^{ES} = \arg(\sum_{l=1}^{N} g_{il} h_l e^{-j\varphi_l}), \tag{9}$$

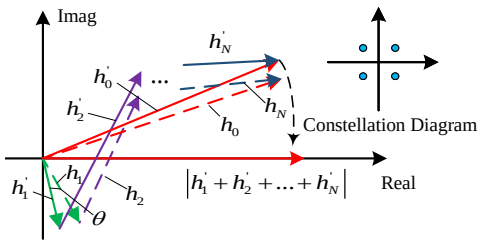

Fig. 2. An illustration of the proposed ERPS/GRPS in principle.

where $\arg(\iota)$ calculates the phase angle of complex scalar ι.

2) GRPS Based Design: With the GRPS, the IRS elements are divided into U groups, and each group consists of $A = N/U$ elements, where U is a non-negative integer power of 2. After that, the phase shifts of the reflecting coefficients are set as $\varphi_{i,t}^u = \varphi_u$ for each IRS group. Subsequently, the signal received by the i-th activated antenna at Bob can be given by

$$y_{bi}^{GS} = \sum_{u=1}^{U}\sum_{t=1}^{A} g_{i,t}^u h_t^u e^{-j\varphi_u} S_k^{GS} + n_{bi}, \tag{10}$$

where, $g_{i,t}^u$ and h_t^u denote the channel from the t-th element of the u-th IRS group to the i-th antenna of Bob and that from Alice to the t-th element of the u-th IRS group, respectively. By following the similar procedures for deriving (8) and (9), at Alice, the transmitted confidential signal S_k^{GS} and the phase of multiplicative perturbation Q_i^{GS} based on GRPS with the i-th receive antenna being activated, are represented as

$$S_k^{GS} = e^{-jQ_i^{GS}} x_k, \tag{11}$$

$$Q_i^{GS} = \arg\Big(\sum_{u=1}^{U}\sum_{t=1}^{A} g_{i,t}^u h_t^u e^{-j\varphi_u}\Big). \tag{12}$$

By incorporating the above, the signal observation of (4) at Bob with RPS schemes, can be rewritten as

$$\mathbf{y}_b = \mathbf{G}\mathbf{\Phi}^m \mathbf{h} S_k^m + \mathbf{n}_b, \tag{13}$$

where $m \in \{ES, GS\}$ corresponds to the ERPS or GRPS. $\mathbf{\Phi}^m$ and S_k^m denote the IRS reflecting coefficient matrix and the transmitted confidential signals, respectively.

Notice that, we can analyze from (7) to (13) that, the GRPS with $U = N$ is actually the ERPS. More specially, due to the independent random variation of cascaded fading channels, the performance results achieved by exploiting the GRPS with different U may remain similar to each other with negligible variance for the same N. In other words, the GRPS schemes with different U except $U = N$ may be capable of achieving nearly the same transmission performance as the ERPS does. To this end, we only need to select the GRPS with single group ($U = 1$) to achieve the best possible transmission performance with the lowest implementation complexity, when the RPS-category schemes are supposed to be utilized.

The schematic mechanism of the ERPS/GRPS based IRS-USRSM with respect to the signal observations at Bob is illustrated with Fig. 2. Here, θ is the phase of the perturbation factor. h_t represents the cascaded channel from Alice to the t-th reflecting element of the IRS, and then to the activated antenna at Bob, while h_t' denotes the cascaded channel with random perturbation, where $t \in \{1, 2, ..., N\}$. h_0 and h_0' represent the synthesized path vectors of the cascaded channel with and without random perturbation, respectively. Eventually, based on employing the ERPS/GRPS, the confidential signals delivered through the perturbed channel paths are observed to be synthesized into a regular constellation pattern at Bob.

B. JTPIR Design Based on RPC

For the RPC based JTPIR, the confidential signal sent by Alice is imposed with a multiplicative perturbation, while the phase-shift of which is updated with the baseband symbol rate. Then, the phase-shift of each IRS reflecting element is carefully adjusted, such that the random perturbation involved with each equivalent cascaded channel path is compensated and hence aligned to the same direction. To do so, the signal constellations achieved by the activate antenna of Bob resembles a regular pattern, while that by arbitrarily selected antenna of Eve retains in disorder.

With RPC, the confidential signal emitted by Alice can be reformulated as

$$S_k^C = w x_k, \tag{14}$$

where $w = e^{-j\theta_1}$ is a random multiplicative perturbation factor with the phase of θ_1, which is updated in $[0, 2\pi)$.

1) ERPC Based Design: According to the principle of the ERPC, the diagonal matrix $\mathbf{\Phi}_i^{EC}$, with the diagonal entries denote the reflecting coefficient configured by the l-th IRS element to the i-th antenna at Bob, is reformulated as

$$\mathbf{\Phi}_i^{EC} = \mathrm{diag}([e^{-j\varphi_{i1}}, e^{-j\varphi_{i2}}, ..., e^{-j\varphi_{il}}, \ldots, e^{-j\varphi_{iN}}]). \tag{15}$$

Then, the phase shift introduced by the l-th IRS element φ_{il} can be designed as

$$\varphi_{il} = -\theta_1 + \angle h_l + \angle g_{il}, \tag{16}$$

where $\angle h_l$ represents the phase of channel h_l, while $\angle g_{il}$ represents the phase of channel g_{il}.

2) GRPC Based Design: Similar to the grouping method used in GRPS, the reflection coefficient vector of each IRS group $\boldsymbol{\varphi}_i^u$, and the diagonal reflection coefficient matrix $\mathbf{\Phi}_i^{GC}$ for the i-th antenna at Bob are respectively denoted as

$$\boldsymbol{\varphi}_i^u = [e^{-j\omega_{i,1}^u}, e^{-j\omega_{i,2}^u}, \ldots, e^{-j\omega_{i,t}^u}, \ldots, e^{-j\omega_{i,A}^u}]^T, \tag{17}$$

$$\mathbf{\Phi}_i^{GC} = \mathrm{diag}\{[(\boldsymbol{\varphi}_i^1)^T, ..., (\boldsymbol{\varphi}_i^u)^T, ..., (\boldsymbol{\varphi}_i^U)^T]\}, \tag{18}$$

where $\omega_{i,t}^u \in (0, 2\pi]$ represents the phase of the t-th element in the u-th group of the IRS. In principle, the reflecting elements in each IRS group share a common reflecting coefficient phase of $\omega_{i,t}^u = \omega_i^u$, which can be expressed as

$$\omega_i^u = \arg\Big(\sum_{t=1}^{A} g_{i,t}^u h_t^u\Big) - \theta_1. \tag{19}$$

Consequently, by aggregating (14), (15) and (18), the received signal (4) at Bob can be reexpressed as

$$\mathbf{y}_b = \mathbf{G}\mathbf{\Phi}_i^n \mathbf{h} S_k^n + \mathbf{n}_b, \tag{20}$$

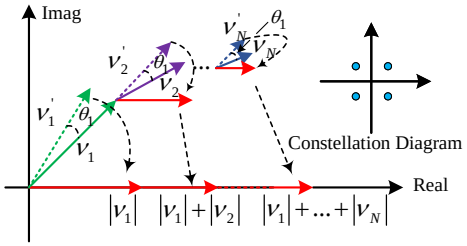

Fig. 3. An illustration of the proposed ERPC/GRPC in principle.

where $n \in \{EC, GC\}$ is short for the ERPC or the GRPC, and $S_k^n = S_k^C$. Specifically, upon utilizing (16) and (19), the received signals of the two schemes can be simplified as

$$y_{bi}^{EC} = \sum_{l=1}^{N} |g_{il}||h_l|x_k + n_{bi}, \tag{21}$$

$$y_{bi}^{GC} = \sum_{u=1}^{U}\sum_{t=1}^{A} |g_{i,t}^u||h_t^u|x_k + n_{bi}. \tag{22}$$

The schematic mechanism of the ERPC/GRPC based IRS-USRSM with respect to the signal observation at Bob is illustrated in Fig. 3. Here, ν_l represents the cascaded channel from Alice to the l-th IRS element, and then to the activated antenna at Bob, while ν_l' represents the cascaded channel multiplied with random perturbation, where $l \in \{1, 2, ..., N\}$. Based on the ERPC/GRPC strategy, the inherent phase disturbance θ_1 introduced for guaranteeing secure transmission can be aligned by the constructive IRS reflection. Ultimately, with signal vector synthesis operations, the random perturbation can be eliminated at the 'activated' antenna of Bob, while remains undissolved at Eve.

Remark 1: The computational complexities of the RPS and RPC based JTPIR schemes can be evaluated via counting the number of complex multiplications consumed by the associated transmitter perturbation and IRS reflection algorithms. From this perspective, we can achieve that the ERPS based scheme possesses higher computational complexity than the GRPS based scheme, which possesses comparable computational complexity to the ERPC/GRPC based schemes. However, based on practical considerations, it is proper to assess the implementation hardware complexity by evaluating the hardware costs for both the signal processing involved computations and the IRS elements associated with fine controlling. Due to this, we can obtain that, the ERPS based scheme has the highest hardware complexity, then the ERPC and GRPS based schemes, while the GRPC based scheme possesses the lowest hardware complexity. Consequently, it is not possible for us to draw the conclusion that, the proposed RPS schemes have lower hardware or implementation complexity than the RPC counterparts. Alternatively, we can draw that, the group-wise RPS/RPC schemes possess lower hardware or implementation complexity than their element-wise counterparts, respectively.

In Table I, in order to represent more clearly the difference between the practicality of the proposed schemes and that of the IRS-RSM scheme, both quantitative and qualitative comparisons are performed to display.

IV. Receiving Signal Detection

In this section, we first introduce the optimal coherent detection of MLD, and then the non-coherent detection of sub-optimal detection (SOD) for the IRS-USRSM systems, so as to fulfil different requirements of detecting complexity. More concretely, in the following, the MLDs are considered and constructed for both receivers of Bob and Eve respectively. Meanwhile, the SOD is merely constructed for Bob since the non-coherent detection is only applicable to Bob, according to the channel assumptions declared in Section II and the above-mentioned JTPIR designs.

A. MLDs

1) MLD at Bob: Given that the MLD is employed at Bob, the detection of activated antenna and APM symbol indices is accomplished jointly. Upon recalling (13) and (20), we can formulate the unified MLD for different JTPIR schemes as

$$\left\langle \hat{i}, \hat{k} \right\rangle = \underset{\tilde{i}\in\mathbb{I},\tilde{k}\in\mathbb{K},}{\arg\min} \|\mathbf{y}_b - \mathbf{G}\mathbf{\Phi}_{\tilde{i}}^o \mathbf{h} S_{\tilde{k}}^o\|^2, \tag{23}$$

where, $\hat{i}$ and $\hat{k}$ represent the estimated indices of the activated antenna and APM symbol, respectively. $\mathbb{I} = \{1, 2, \ldots, N_b\}$, $\mathbb{K} = \{1, 2, \ldots, M\}$, and $o \in \{ES, EC, GS, GC\}$.

2) MLD at Eve: Since in either scenario of $\mathcal{I}$ or $\mathcal{J}$, the signals observed at Eve are inevitably contaminated by random interferences. Then, opposite from that done at Bob, APM-resembled constellation pattern is away from being synthesised at Eve. Due to this, we can barely formulate the MLD at Eve upon utilizing (5) and (6) as

$$\hat{k} = \underset{\tilde{k}\in\mathbb{K}}{\arg\min} \|\mathbf{y}_e - |\mathbf{y}_e^s| S_{\tilde{k}}\|^2, \tag{24}$$

where $s \in \{\mathcal{I}, \mathcal{J}\}$. As the inherent perturbations merged in $S_{\tilde{k}}$ retains unknown for Eve, it is merely possible to achieve correct detection of $\hat{k}$, not even mention that of $\hat{i}$. Eventually, with the MLD, the BER achieved at Eve is about 0.5.

B. SOD at Bob

In this subsection, we propose a two-stage SOD, so as to decrease the computational complexity of detection at Bob, whilst retaining a BER performance comparable to that by MLD.

1) Activate Antenna Index Detection: Due to principle, the activated antenna is capable of yielding the highest receiving power among all the antennas at Bob. To this end, in the first stage, the detection of $\hat{i}$ at Bob can be articulated as

$$\hat{i} = \underset{\tilde{i}\in\mathbb{I}}{\arg\max}\{|y_{b\tilde{i}}|^2\}, \tag{25}$$

where $y_{b\tilde{i}}$ is the $\tilde{i}$-th element of $\mathbf{y}_b$.

2) APM Symbol Index Detection: Based on the detection of $\hat{i}$, the baseband APM symbol index can be detected as

$$\hat{k} = \underset{\tilde{k}\in\mathbb{K}}{\arg\min}\, 2\Re\{y_{b\hat{i}}\mathbf{G}\mathbf{\Phi}_{\hat{i}}^o \mathbf{h} w x_{\tilde{k}} + \sum_{i,i\neq\hat{i}} (y_{bi}\mathbf{G}\mathbf{\Phi}_{\hat{i}}^o \mathbf{h} w x_{\tilde{k}} - \left\|\mathbf{G}\mathbf{\Phi}_{\hat{i}}^o \mathbf{h} w x_{\tilde{k}}\right\|^2)\}. \tag{26}$$

By analyzing (23), (25) and (26), we can obtain the computational complexity of MLD as $\mathcal{O}(MNUN_b)$, while that of

TABLE I
QUANTITATIVE AND QUALITATIVE COMPARISON BETWEEN DIFFERENT JTPIR SCHEMES AND THE IRS-RSM WITH $N_t = 1$, $N_b = 2$, $N = 64$, $U = 2$ AND $M = 4$.

Transmission Scheme	Qualitative Comparison			Quantitative Comparison
	Hardware Complexity	Runtime	Additional Power Consumption	Computational Complexity
ERPS Based JTPIR	Highest	★★★★★★	No	$\mathcal{O}(2NN_b)$
GRPS Based JTPIR	Medium	★★★	No	$\mathcal{O}(UAN_b)$
ERPC Based JTPIR	High	★★★	No	$\mathcal{O}(NN_b)$
GRPC Based JTPIR	Low	★★★	No	$\mathcal{O}(UAN_b)$
IRS-RSM	High	★★★	No	$\mathcal{O}(NN_b)$

SOD algorithm as $\mathcal{O}(N_b + MN)$. However, given the RPS based JTPIR is exploited, the error introduced to the non-coherent detection of SOD is unexpectedly large, which leads to the unreliable detection of first $\hat{i}$ and then $\hat{k}$. Therefore, in the following, only the IRS-USRSM systems with RPC based JTPIR and the MLD/SOD is explored.

V. SECRECY PERFORMANCE EVALUATION

In this section, we analyse the secrecy performance of the IRS-USRSM system by evaluating the ABEP and DCMCC performance discrepancy between the receivers of Bob and Eve. To evaluate the best achieved secrecy performance, the transmission of ERPC based JTPIR and the detection of MLD are considered. Specifically, we employ the analysis method of MGF and CLT to form a general framework, so as to facilitate the derivation of ABEP and DCMCC results [37].

A. ABEP Discrepancy

In this subsection, we investigate the discrepancy between ABEP performance achieved by Bob and Eve.

1) Discrepancy Evaluation: The ABEP achieved by the IRS-USRSM with MLD can be given by [1]

$$\bar{P} = \zeta \mathbb{E}_{\mathbf{G},\mathbf{h}}[\sum_{i=1}^{N_b}\sum_{k=1}^{M}\sum_{\hat{i}=1}^{N_b}\sum_{\hat{k}=1}^{M} d(\mathbf{r}_{i,k}, \mathbf{r}_{\hat{i},\hat{k}}) P\{\mathbf{r}_{i,k}, \mathbf{r}_{\hat{i},\hat{k}}|\mathbf{G},\mathbf{h}\}] \tag{27}$$

where, $\zeta = \frac{1}{MN_b \log_2(MN_b)}$, $\mathbf{r}_{i,k} = \mathbf{G}\mathbf{\Phi}_i^o \mathbf{h} S_k^o$, $\mathbf{r}_{\hat{i},\hat{k}} = \mathbf{G}\mathbf{\Phi}_{\hat{i}}^o \mathbf{h} S_{\hat{k}}^o$, $\mathbb{E}_{\mathbf{G},\mathbf{h}}[\cdot]$ is the expectation operator, $d(\mathbf{r}_{i,k}, \mathbf{r}_{\hat{i},\hat{k}})$ calculates the Hamming distance between the symbol representations, and $P\{\mathbf{r}_{i,k}, \mathbf{r}_{\hat{i},\hat{k}}|\mathbf{G},\mathbf{h}\}$ denotes the conditional pairwise error probability (PEP). Due to the involvement of multiple integrals in (27), further simplification of it becomes difficult. Fortunately, with the Jensen's inequality, we can achieve the ABEP union-bound (ABEP-UB) from (27) as

$$\bar{P}_{UB} = \zeta \sum_{i=1}^{N_b}\sum_{k=1}^{M}\sum_{\hat{i}=1}^{N_b}\sum_{\hat{k}=1}^{M} d(\mathbf{r}_{i,k}, \mathbf{r}_{\hat{i},\hat{k}}) \mathbb{E}_{\mathbf{G},\mathbf{h}}[P\{\mathbf{r}_{i,k}, \mathbf{r}_{\hat{i},\hat{k}}|\mathbf{G},\mathbf{h}\}] \tag{28}$$

where, the conditional PEP can be expressed as [38]

$$\begin{aligned} &P\{\mathbf{r}_{i,k}, \mathbf{r}_{\hat{i},\hat{k}}|\mathbf{G},\mathbf{h}\} \\ &= P\{||\mathbf{y}_b - \mathbf{G}\mathbf{\Phi}_i^{EC}\mathbf{h}wx_k||^2 > ||\mathbf{y}_b - \mathbf{G}\mathbf{\Phi}_i^{EC}\mathbf{h}wx_{\hat{k}}||^2\} \\ &= P(-||x_k \sum_{l}^{N} |h_l||g_{il}| - g_{\hat{i}l}\mathbf{\Phi}_i^{EC}\mathbf{h}wx_{\hat{k}}||^2 \\ &\quad -2\Re\{(x_k \sum_{l}^{N} |h_l||g_{il}| - g_{\hat{i}l}\mathbf{\Phi}_i^{EC}\mathbf{h}wx_{\hat{k}})\} > 0). \end{aligned} \tag{29}$$

By employing the Q-function [39], we can simplify (29) as

$$\begin{aligned} &P\{\mathbf{r}_{i,k}, \mathbf{r}_{\hat{i},\hat{k}}|\mathbf{G},\mathbf{h}\} \\ &= Q(\sqrt{\frac{||\mathbf{G}\mathbf{\Phi}_i^{EC}\mathbf{h}wx_k - \mathbf{G}\mathbf{\Phi}_i^{EC}\mathbf{h}wx_{\hat{k}}||^2}{2\sigma_b^2}}) = Q(\sqrt{\frac{\xi}{2\sigma_b^2}}), \end{aligned} \tag{30}$$

where $Q(x) = \frac{1}{\sqrt{2\pi}}\int_x^\infty \exp(-\frac{t^2}{2})dt$, $\xi = ||\mathbf{G}\mathbf{\Phi}_i^{EC}\mathbf{h}wx_k - \mathbf{G}\mathbf{\Phi}_i^{EC}\mathbf{h}wx_{\hat{k}}||^2$. Further, with an alternation of the Q-function [37], the unconditional PEP can be expressed as

$$\bar{P}\{\mathbf{r}_{i,k}, \mathbf{r}_{\hat{i},\hat{k}}\} = \mathbb{E}_{\mathbf{G},\mathbf{h}}[Q(\sqrt{\frac{\xi}{2\sigma_b^2}})] = \frac{1}{\pi}\int_0^{\frac{\pi}{2}} M_\xi(\omega)d\eta, \tag{31}$$

where $M_\xi(\cdot)$ denotes the MGF of ξ, $\omega = -1/(4\sin^2\eta\sigma_b^2)$. Let us introduce a tight upper bound on the Q-function in (30) as

$$Q(\sqrt{\frac{\xi}{2\sigma_b^2}}) \leq \sum_{n=1}^{3} \alpha_n e^{-\frac{\xi}{\gamma_n\sigma_b^2}}, \tag{32}$$

where $[\alpha_1, \alpha_2, \alpha_3] = [\frac{1}{6}, \frac{1}{12}, \frac{1}{4}]$, $[\gamma_1, \gamma_2, \gamma_3] = [1, 2, 4]$. Then, the unconditional PEP is depicted to be upper-bounded as

$$\bar{P}\{\mathbf{r}_{i,k}, \mathbf{r}_{\hat{i},\hat{k}}\} \leq \mathbb{E}_{\mathbf{G},\mathbf{h}}[\sum_{n=1}^{3}\alpha_n e^{\tau\xi}] = \sum_{n=1}^{3}\alpha_n M_\xi(\tau), \tag{33}$$

where $\tau = -1/(\gamma_n\sigma_b^2)$. Hence, we can achieve the ABEP upper-bound (ABEP-UPB) of the considered IRS-USRSM as

$$\bar{P}_{UPB} = \zeta \sum_{i}\sum_{\hat{i}}\sum_{k}\sum_{\hat{k}} d(\mathbf{r}_{i,k}, \mathbf{r}_{\hat{i},\hat{k}}) \sum_{n=1}^{3}\alpha_n M_\xi(\tau). \tag{34}$$

Notice that, due to the random perturbations and RPS/RPC based reflections utilized, the signal constellation synthesized at Eve is always disrupted, resulting in that Eve's bit error rate retains around 0.5 with slight variations. To this end, we only need to derive the ABEP performance of $\bar{P}_{UB}$ in (28) or $\bar{P}_{UPB}$ in (34), to accomplish the ABEP discrepancy evaluation. By substituting (31) into (28) or analyzing (34), the issue that hinges the evaluation of ABEP discrepancy is the further simplification of $M_\xi(\cdot)$. Hence, in the remaining part of this subsection, we focus on deriving closed-form MGF for ξ.

2) MGF Derivation: According to the mapping and modulating rules elaborated in Section II-B, there are three categories of detection errors at Bob. As a result, the variable ξ is divided into three cases of $\xi_1 = \{\xi|\hat{i} = i, \hat{k} \neq k\}$, $\xi_2 = \{\xi|\hat{i} \neq i, \hat{k} = k\}$, and $\xi_3 = \{\xi|\hat{i} \neq i, \hat{k} \neq k\}$. Since the parameter variables ξ_1, ξ_2 and ξ_3 obey different statistical distributions, to accomplish the accurate derivation of $M_\xi(\cdot)$, the MGFs of ξ_1, ξ_2, and ξ_3 are deduced separately as follows.

i) $\xi_1 = \{\xi|\hat{i} = i, \hat{k} \neq k\}$:

In this case, ξ_1 can be further expressed as

$$\begin{aligned}\xi_1 &= |x_k - x_{\hat{k}}|^2 \sum_{m}^{N_b} |\sum_{l=1}^{N} |h_l||g_{ml}|e^{j(\angle g_{il} - \angle g_{ml})}|^2 \\ &= \underbrace{|x_k - x_{\hat{k}}|^2 \sum_{m=1, m\neq i}^{N_b} |\sum_{l=1}^{N} |h_l||g_{ml}|e^{j(\angle g_{il} - \angle g_{ml})}|^2}_{\xi_{11}} \\ &\quad + \underbrace{|x_k - x_{\hat{k}}|^2 |\sum_{l=1}^{N} |h_l||g_{il}||^2}_{\xi_{12}}.\end{aligned} \tag{35}$$

To further analyze the MGF of ξ_1, we define u_{ml} and v_{ml} as the real and imaginary parts of $|h_l||g_{ml}|e^{j(\angle g_{il} - \angle g_{ml})}$, respectively, i.e., $u_m = \sum_{l=1}^{N} u_{ml}$, $v_m = \sum_{l=1}^{N} v_{ml}$. Then, ξ_1 can be reexpressed as the sum of $\xi_{11} = |x_k - x_{\hat{k}}|^2 \sum_{m=1, m\neq i}^{N_b} ({u_m}^2 + {v_m}^2)$ and $\xi_{12} = |x_k - x_{\hat{k}}|^2 |\sum_{l=1}^{N} |h_l||g_{il}||^2$. Given $m \neq i$, according to the CLT, we have that ξ_{11} follows the generalized central chi-square distribution with $2(N_b - 1)$ degree-of-freedom (DoF), while the mean and variance of $\sum_{l=1}^{N} |h_l||g_{ml}|e^{j(\angle g_{il} - \angle g_{ml})}$ as

$$N\mathbb{E}[|h_l||g_{ml}|e^{j(\angle g_{il} - \angle g_{ml})}] = 0, \tag{36}$$

$$N\mathbb{D}[|h_l||g_{ml}|e^{j(\angle g_{il} - \angle g_{ml})}] = N. \tag{37}$$

Consequently, the associated MGF can be deduced as

$$M_{\xi_{11}}(t) = (1 - tN|x_k - x_{\hat{k}}|^2)^{-(N_b - 1)}. \tag{38}$$

Given $m = i$, with the CLT, ξ_{12} is inferred to subject to the generalized non-central chi-square distribution, while $\sum_{l=1}^{N} |h_l||g_{ml}|$ can be approximated as a Gaussian random variable, with the mean and variance of $(\pi N)/4$ and $(16 - \pi^2)N/16$, respectively. Rendering that the MGF of generalized non-central chi-square distribution is defined as

$$\begin{aligned}M_X(t|\boldsymbol{\mu}, \mathbf{C}) &= [\det(\mathbf{E} - 2t\mathbf{C})]^{-\frac{1}{2}} \\ &\quad \times \exp\{-\tfrac{1}{2}\boldsymbol{\mu}^{\mathrm{T}}[\mathbf{E} - (\mathbf{E} - 2t\mathbf{C})^{-1}]\mathbf{C}^{-1}\boldsymbol{\mu}\},\end{aligned} \tag{39}$$

where, $X = \sum_{i=1}^{n} X_i^2$, $\mathbf{E}$ denotes the identity matrix, and $\boldsymbol{\mu}$ and $\mathbf{C}$ are the mean vector and covariance matrix of $[X_1, X_2, ..., X_n]^{\mathrm{T}}$. Then, we let $\mu_1 = \frac{\pi N}{4}|x_k - x_{\hat{k}}|$, $C_1 = \frac{16-\pi^2}{16}N|x_k - x_{\hat{k}}|^2$, and have the MGF of ξ_{12} as

$$M_{\xi_{12}}(t|\mu_1, C_1) = M_{\xi_{12}}(t|\frac{\pi}{4}N|x_k - x_{\hat{k}}|, \frac{16-\pi^2}{16}N|x_k - x_{\hat{k}}|^2). \tag{40}$$

Finally, due to the independence between ξ_{11} and ξ_{12}, the integral MGF of ξ_1 is given as

$$M_{\xi_1}(t) = M_{\xi_{11} + \xi_{12}}(t) = M_{\xi_{11}}(t)M_{\xi_{12}}(t). \tag{41}$$

ii) $\xi_2 = \{\xi | \hat{i} \neq i, \hat{k} = k\}$:
Similarly, in this case, we first express ξ_2 as

$$\xi_2 = \sum_{m}^{N_b} |\sum_{l=1}^{N} |h_l||g_{ml}|x_k(e^{j(\angle g_{il} - \angle g_{ml})} - e^{j(\angle g_{\hat{i}l} - \angle g_{ml})})|^2. \tag{42}$$

Then, we separate ξ_2 into two independent parts of ξ_{21} and ξ_{22}, where $\xi_{22} = \xi_{221} + \xi_{222}$, and formulate these as follows.

$$\xi_{21} = \sum_{m\neq i,\hat{i}}^{N_b} |\sum_{l=1}^{N} |h_l||g_{ml}|x_k(e^{j(\angle g_{il} - \angle g_{ml})} - e^{j(\angle g_{\hat{i}l} - \angle g_{ml})})|^2, \tag{43}$$

$$\xi_{221} \overset{m=i}{=} |\sum_{l=1}^{N} |h_l||g_{il}|x_k(1 - e^{j(\angle g_{\hat{i}l} - \angle g_{il})})|^2, \tag{44}$$

$$\xi_{222} \overset{m=\hat{i}}{=} |\sum_{l=1}^{N} |h_l||g_{\hat{i}l}|x_k(e^{j(\angle g_{il} - \angle g_{\hat{i}l})} - 1)|^2, \tag{45}$$

where ξ_{21} also follows the generalized central chi-square distribution with $2(N_b - 2)$ DoF, and the MGF as

$$M_{\xi_{21}}(t) = [1 - tN|x_k|^2]^{-(N_b - 2)}. \tag{46}$$

Let $x_k = a_k + b_k$, $x_{\hat{k}} = a_{\hat{k}} + b_{\hat{k}}$, we utilize the method adopted in case *i)*, and derive the mean vector and covariance matrix for ξ_{22} as

$$\boldsymbol{\mu}_2 = [u_i, v_i, u_{\hat{i}}, v_{\hat{i}}]^T = \frac{\pi}{4}N[a_k, b_k, -a_k, -b_k]^T, \tag{47}$$

$$\mathbf{C}_2 = N \begin{bmatrix} \sigma_{11}^2 & \sigma_{12}^2 & \sigma_{13}^2 & \sigma_{14}^2 \\ \sigma_{12}^2 & \sigma_{22}^2 & \sigma_{23}^2 & \sigma_{24}^2 \\ \sigma_{13}^2 & \sigma_{23}^2 & \sigma_{33}^2 & \sigma_{34}^2 \\ \sigma_{14}^2 & \sigma_{24}^2 & \sigma_{34}^2 & \sigma_{44}^2 \end{bmatrix}, \tag{48}$$

where

$$\begin{aligned}&\sigma_{11}^2 = \sigma_{33}^2 = \tfrac{16-\pi^2}{16}a_k^2 + \tfrac{|x_k|^2}{2}, \sigma_{22}^2 = \sigma_{44}^2 = \tfrac{16-\pi^2}{16}b_k^2 + \tfrac{|x_k|^2}{2}, \\ &\sigma_{12}^2 = \sigma_{34}^2 = \tfrac{16-\pi^2}{16}a_k b_k, \sigma_{13}^2 = (\tfrac{\pi^2}{16} - \tfrac{3\pi}{8})a_k^2 + \tfrac{\pi}{8}b_k^2, \\ &\sigma_{14}^2 = \sigma_{23}^2 = (\tfrac{\pi^2}{16} - \tfrac{\pi}{2})a_k b_k, \sigma_{24}^2 = (\tfrac{\pi^2}{16} - \tfrac{3\pi}{8})b_k^2 + \tfrac{\pi}{8}a_k^2.\end{aligned} \tag{49}$$

Consequently, by substituting (47) and (48) into (39), the MGF of ξ_{22} can be obtained as

$$\begin{aligned}M_{\xi_{22}}(t|\mu_2, \mathbf{C}_2) &= [\det(\mathbf{E} - 2t\mathbf{C}_2)]^{-\frac{1}{2}} \\ &\quad \times \exp\{-\tfrac{1}{2}{\mu_2}^{\mathrm{T}}[\mathbf{E} - (\mathbf{E} - 2t\mathbf{C}_2)^{-1}]{\mathbf{C}_2}^{-1}\mu_2\}.\end{aligned} \tag{50}$$

Finally, similar to (41), we have $M_{\xi_2}(t) = M_{\xi_{21}}(t)M_{\xi_{22}}(t)$.

iii) $\xi_3 = \{\xi | \hat{i} \neq i, \hat{k} \neq k\}$:
To begin with, let us divide

$$\xi_3 = \sum_{m}^{N_b} |\sum_{l=1}^{N} |h_l||g_{ml}|(x_k e^{j(\angle g_{il} - \angle g_{ml})} - x_{\hat{k}} e^{j(\angle g_{\hat{i}l} - \angle g_{ml})})|^2 \tag{51}$$

into two independent partials as ξ_{31} and ξ_{32}, where $\xi_{32} = \xi_{321} + \xi_{322}$, and formulate them as follows.

$$\begin{aligned}\xi_{31} = \sum_{m=1, m\neq i,\hat{i}}^{N_r} |\sum_{l=1}^{N} |h_l||g_{ml}|(x_k e^{j(\angle g_{il} - \angle g_{ml})} \\ - x_{\hat{k}} e^{j(\angle g_{\hat{i}l} - \angle g_{ml})})|^2,\end{aligned} \tag{52}$$

$$\begin{aligned}\xi_{31} = \sum_{m=1, m\neq i,\hat{i}}^{N_r} |\sum_{l=1}^{N} |h_l||g_{ml}|(x_k e^{j(\angle g_{il} - \angle g_{ml})} \\ - x_{\hat{k}} e^{j(\angle g_{\hat{i}l} - \angle g_{ml})})|^2,\end{aligned} \tag{53}$$

$$\xi_{322} \overset{m=\hat{i}}{=} |\sum_{l=1}^{N} |h_l||g_{\hat{i}l}|(x_k e^{j(\angle g_{il} - \angle g_{\hat{i}l})} - x_{\hat{k}})|^2. \tag{54}$$

By applying the methodology introduced in case *i)*, one can have the MGF of ξ_{31} be deduced as

$$M_{\xi_{31}}(t) = [1 - tN(|x_k|^2 + |x_{\hat{k}}|^2)]^{-(N_b-2)}. \tag{55}$$

Denote the mean vector and covariance matrix for ξ_{32} as

$$\boldsymbol{\mu}_3 = \frac{\pi}{4} N[a_k, b_k, -a_{\hat{k}}, -b_{\hat{k}}]^T, \tag{56}$$

$$\mathbf{C}_3 = N \begin{bmatrix} \sigma_{11}^2 & \sigma_{12}^2 & \sigma_{13}^2 & \sigma_{14}^2 \\ \sigma_{12}^2 & \sigma_{22}^2 & \sigma_{23}^2 & \sigma_{24}^2 \\ \sigma_{13}^2 & \sigma_{23}^2 & \sigma_{33}^2 & \sigma_{34}^2 \\ \sigma_{14}^2 & \sigma_{24}^2 & \sigma_{34}^2 & \sigma_{44}^2 \end{bmatrix}, \tag{57}$$

where

$$\begin{aligned} &\sigma_{11}^2 = 0, \sigma_{22}^2 = \tfrac{16-\pi^2}{16} b_k^2 + \tfrac{|x_{\hat{k}}|^2}{2}, \\ &\sigma_{33}^2 = \tfrac{16-\pi^2}{16} a_{\hat{k}}^2 + \tfrac{|x_k|^2}{2}, \sigma_{44}^2 = \tfrac{16-\pi^2}{16} b_{\hat{k}}^2 + \tfrac{|x_k|^2}{2}, \\ &\sigma_{12}^2 = \tfrac{16-\pi^2}{16} a_k b_k, \sigma_{13}^2 = (\tfrac{\pi^2}{16} - \tfrac{3\pi}{8}) a_k a_{\hat{k}} + \tfrac{\pi}{8} b_k b_{\hat{k}}, \\ &\sigma_{14}^2 = (\tfrac{\pi^2}{16} - \tfrac{3\pi}{8}) a_k b_{\hat{k}} - \tfrac{\pi}{8} a_{\hat{k}} b_{\hat{k}}, \sigma_{23}^2 = (\tfrac{\pi^2}{16} - \tfrac{3\pi}{8}) a_{\hat{k}} b_k - \tfrac{\pi}{8} a_k b_{\hat{k}}, \\ &\sigma_{24}^2 = (\tfrac{\pi^2}{16} - \tfrac{3\pi}{8}) b_k b_{\hat{k}} + \tfrac{\pi}{8} a_k a_{\hat{k}}, \sigma_{34}^2 = \tfrac{16-\pi^2}{16} a_{\hat{k}} b_{\hat{k}}. \end{aligned} \tag{58}$$

Then, the MGF of ξ_{32} can be written as

$$\begin{aligned} M_{\xi_{32}}(t|\mu_3, \mathbf{C}_3) &= [\det(\mathbf{E} - 2t\mathbf{C}_3)]^{-\frac{1}{2}} \\ &\times \exp\{-\tfrac{1}{2}{\mu_3}^{\mathrm{T}}[\mathbf{E} - (\mathbf{E} - 2t\mathbf{C}_3)^{-1}]{\mathbf{C}_3}^{-1}\mu_3\}. \end{aligned} \tag{59}$$

Finally, we have $M_{\xi_3}(t) = M_{\xi_{31}}(t) M_{\xi_{32}}(t)$.

By substituting the outcomes $M_{\xi_1}(t)$, $M_{\xi_2}(t)$, and $M_{\xi_3}(t)$ into (31) and (33), the unconditional PEP and its upper-bound for each case can be obtained. Further, combining the unconditional PEP results with (28) and (34), we achieve the closed-form ABEP-UB for each case as

$$\bar{P}_{UB}^{\xi_1} = \frac{\zeta N_b}{\pi} \sum_k \sum_{\hat{k}} d(k, \hat{k}) \int_0^{\frac{\pi}{2}} M_{\xi_1}(\omega) d\eta, \tag{60}$$

$$\bar{P}_{UB}^{\xi_2} = \frac{\zeta M}{\pi} \sum_i \sum_{\hat{i}} d(i, \hat{i}) \int_0^{\frac{\pi}{2}} M_{\xi_2}(\omega) d\eta, \tag{61}$$

$$\bar{P}_{UB}^{\xi_3} = \frac{\zeta}{\pi} \sum_i \sum_{\hat{i}} \sum_k \sum_{\hat{k}} d(\{i,k\}, \{\hat{i}, \hat{k}\}) \int_0^{\frac{\pi}{2}} M_{\xi_3}(\omega) d\eta, \tag{62}$$

while the closed-form ABEP-UPB for each case as

$$\bar{P}_{UPB}^{\xi_1} = \zeta N_b \sum_k \sum_{\hat{k}} d(k, \hat{k}) \sum_{n=1}^{3} \alpha_n M_{\xi_1}(\tau), \tag{63}$$

$$\bar{P}_{UPB}^{\xi_2} = \zeta M \sum_i \sum_{\hat{i}} d(i, \hat{i}) \sum_{n=1}^{3} \alpha_n M_{\xi_2}(\tau), \tag{64}$$

$$\bar{P}_{UPB}^{\xi_3} = \zeta \sum_i \sum_{\hat{i}} \sum_k \sum_{\hat{k}} d(\{i,k\}, \{\hat{i}, \hat{k}\}) \sum_{n=1}^{3} \alpha_n M_{\xi_3}(\tau). \tag{65}$$

Eventually, according to definitions given by (28) and (34), the ABEP-UB and ABEP-UPB results are actually the sum of the ABEP-UB and ABEP-UPB results corresponding to all the pairwise error cases. In summary, the performance results of $\bar{P}_{UB}$ and $\bar{P}_{UPB}$ can be calculated with the summations of ((60)-(62) and (63)-(65), respectively.

B. Achievable ESR

In this subsection, we analyze the achieved ESR R_s of the IRS-USRSM system with ERPC based JTPIR and the MLD, which is defined as

$$R_s = [R_b - R_e]^+, \tag{66}$$

where R_b and R_e are the information transmission rate and information leakage rate, which are derived by the DCMCCs of Bob and Eve, respectively.

1) DCMCC at Bob: For the given IRS-USRSM system, the DCMCC at Bob R_b can be written as

$$R_b = \mathbb{E}_{\mathbf{G},\mathbf{h}}[I(x_k; \mathbf{y}_b | \mathbf{G}, \mathbf{h})], \tag{67}$$

where $I(x; y|z)$ denotes the mutual information between the random variables x and y with the given condition of z.

Theorem 1: R_b in (67) can be approximated by

$$\begin{aligned} \tilde{R}_b = &\log_2(N_b M) + N_b - N_b/\ln 2 \\ &- \frac{1}{N_b M} \sum_{i,k} \log_2 \sum_{\hat{i},\hat{k}} M_\xi(-\frac{1}{2\sigma_b^2}). \end{aligned} \tag{68}$$

Proof 1: See Appendix A. ■

Finally, we can derive the closed-form $\tilde{R}_b$ by substituting the MGF result $M_\xi(\cdot)$ achieved in Section V-A into (68).

2) DCMCC at Eve: To evaluate the ideal DCMCC at Eve, we assume that Eve could always obtain the complete CSI and multiplicative perturbation. Then, a simplification of R_e is provided with a theorem in general. Then, by introducing distribution approximating method, we elaborate with another theorem to detail the closed-form upper-bounds for R_e with respect to specific eavesdropping scenarios of $\mathcal{I}$ and $\mathcal{J}$.

Theorem 2: The DCMCC at Eve R_e can be simplified as

$$\begin{aligned} R_e = &\log_2 M - N_e/\ln 2 \\ &- \frac{1}{M} \sum_{k=1}^{M} \mathbb{E}_{\mathbf{U},\mathbf{n}_e}[\log_2 \sum_{k'=1}^{M} \exp(-\frac{||\mathbf{U}(x_k - x_{\hat{k}}) + \mathbf{n}_e||^2}{{\sigma_e}^2})], \end{aligned} \tag{69}$$

Proof 2: See Appendix B. ■

Theorem 3: The closed-form upper-bound of $R_e^{\mathcal{I}}$ can be given by

$$\begin{aligned} R_e^{\mathcal{I}} \le &\log_2 M + N_e - N_e/\ln 2 \\ &- \frac{1}{M} \sum_{k=1}^{M} \log_2 \sum_{k'=1}^{M} (1 + \frac{|x_k - x_{\hat{k}}|^2}{2{\sigma_e}^2})^{-N_e}. \end{aligned} \tag{70}$$

By contrast, the upper-bound of $R_e^{\mathcal{J}}$ is given by

$$R_e^{\mathcal{J}} \le \tilde{R}_e^{\mathcal{J},1}, \tag{71}$$

$$R_e^{\mathcal{J}} \le \tilde{R}_e^{\mathcal{J},2}, \tag{72}$$

where $\tilde{R}_e^{\mathcal{J},1}$ and $\tilde{R}_e^{\mathcal{J},2}$ are denoted by (84) and (85), which are achieved with closed-form upon utilizing the gamma approximation as per signal-to-noise ratio (SNR) point manner and high SNR approximation manner, respectively.

Proof 3: See Appendix C. ■

Eventually, upon invoking (66), the closed-form ESR lower bounds $\bar{R}_s^{\mathcal{I}}$, $\bar{R}_s^{\mathcal{J},1}$ and $\bar{R}_s^{\mathcal{J},2}$ can be achieved by substituting $\tilde{R}_b$ in *Theorem* 1 and $\tilde{R}_e^{\mathcal{I}}$, $\tilde{R}_e^{\mathcal{J},1}$, $\tilde{R}_e^{\mathcal{J},2}$ in *Theorem* 3 into (66), respectively.

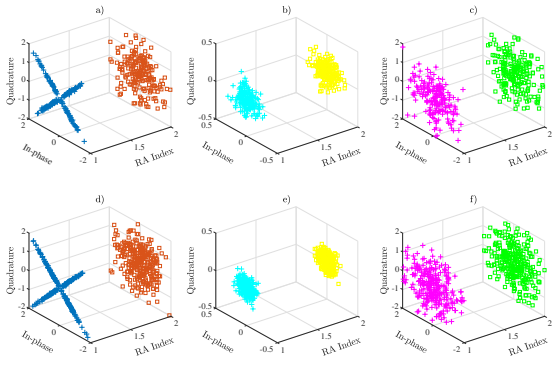

Fig. 4. 3D constellations for IRS-USRSM systems with JTPIR based on RPS. a) ERPS, Bob; b) ERPS, Eve in scenario $\mathcal{I}$; c) ERPS, Eve in scenario $\mathcal{J}$; d), e), and f) are for GRPS with the same cases of a), b), and c), respectively.

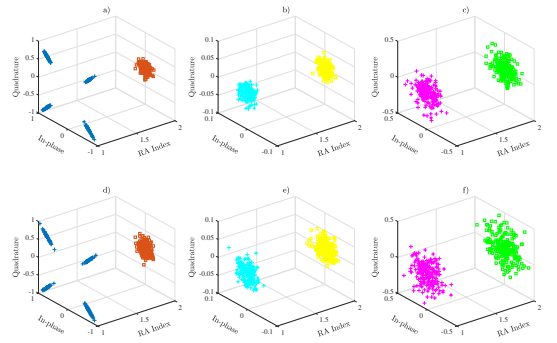

Fig. 5. 3D constellations for IRS-USRSM systems with JTPIR based on RPC. a) ERPC, Bob; b) ERPC, Eve in scenario $\mathcal{I}$; c) ERPC, Eve in scenario $\mathcal{J}$; d), e), and f) are for GRPC with the same cases of a), b), and c), respectively.

VI. Simulation and Discussions

In this section, we depict and compare the BER and DCMCC results of the uplink communications systems assisted by our proposed IRS-USRSM and other counterparts and benchmark schemes, so as to demonstrate the efficiency of our technical proposal with regard to security enhancing. We illustrate the simulation in the following four aspects:*1) Illustration of 3D Received Constellations; 2) BER Comparison of the IRS-USRSM Systems; 3) BER and ESR Comparisons of Different Uplink Transmissions; 4) Comparison of Simulated/Analytical BERs and DCMCCs.* To be specific, we begin by comparing the 3D constellation scatter plots achieved by both receivers of Bob and Eve, respectively. Second, we characterize the simulated BER results to demonstrate the performance differences of the proposed IRS-USRSM systems with different transceive scheme combinations and communication resource configurations. Furthermore, we show the simulated BER attainable by either receiver of the proposed IRS-USRSM and other benchmark systems. Finally, we demonstrate both simulated and theoretical BER and DCMCC performance results to verify the correctness of our analytical derivation. Note that the configuration parameters of the explored systems are given in the caption of the figures.

A. Illustration of 3D Received Constellations

In Fig. 4, we demonstrate the 3D constellations observed at Bob and Eve with ERPS and GRPS based JTPIR, respectively. The system parameters are set as $N_t = 1$, $N_b = 2$, $N = 64$, $U = 2$, and $M = 4$, with a SNR of 5 dB. The index of desired receiving antenna is chosen as 1. From Fig. 4 we can have that, by utilizing either the ERPS or GRPS, Bob is able to achieve a regular constellation observation, while Eve is only able to observe scrambled constellations. This is due to the fact that, with the RPS scheme, the multiplicative perturbation can be eliminated by vector synthesis at Bob with superior BER performance, while at Eve, the multiplicative perturbation cannot be rectified, which results in the scrambled signal observations and the extremely poor BER performance. Furthermore, the amplitude of the scrambled constellation diagram for Eve in Scenario $\mathcal{I}$ is significantly smaller than that in Scenario $\mathcal{J}$. This is because Eve in Scenario $\mathcal{J}$ can receive the interfering (jamming) signal reflected from the IRS, which elevates the amplitude range of the receiving signals. However, due to the indissoluble multiplicative perturbation, the obtained constellations at Eve remain in messy, and also the BER performance is poor. Our results clearly validate that IRS-USRSM is capable for guaranteeing secure and efficient uplink transmission against passive eavesdropping.

In Fig. 5, we characterize the 3D constellations achieved at Bob and Eve in IRS-USRSM system with ERPC and GRPC based JTPIR respectively, where the system parameters are set the same as in Fig. 4. From Fig. 5 we can observe that, by employing either the ERPC or GRPC, Bob can achieve regular constellation observations, while Eve can only attain disordered constellation patterns. This is simply because, the IRS based phase alignment manipulations are able to remove the multiplicative perturbation at Bob, while augmenting the disorderedness of the signal received at Eve. Meanwhile, the amplitude of the constellation pattern of Eve in Scenario $\mathcal{I}$ is significantly smaller than that in Scenario $\mathcal{J}$. Furthermore, by comparing Fig. 4 with Fig. 5, that the amplitudes of the constellation pattern at Bob with the RPC-category schemes are consistently larger than that with the RPS-category counterparts. This is due to that when compared with the ERPS scheme, the IRS based phase alignment operations implemented with the ERPC are capable of yielding a larger signal power at Bob, also a resultant better BER. Moreover, upon utilizing the IRS grouping manipulations, the quality of the receiving signals achieved with the GRPS and GRPC schemes are degraded uniformly. These in all demonstrate the security and efficiency of the proposed scheme, as well as convince us that the proposed IRS-USRSM can be exploited for assisting the promising construction of wireless secure IoT communications.

B. BER Comparison of the IRS-USRSM Systems

In Fig. 6, we characterize the BER performance achieved by Bob and Eve for the GRPS based IRS-USRSM systems with different N, U, and eavesdropping scenarios. It can be seen from Fig. 6 that Eve's BER performance retains around 0.5 for all the investigated systems. Second, Bob's BER performance improves gradually as N increases. This

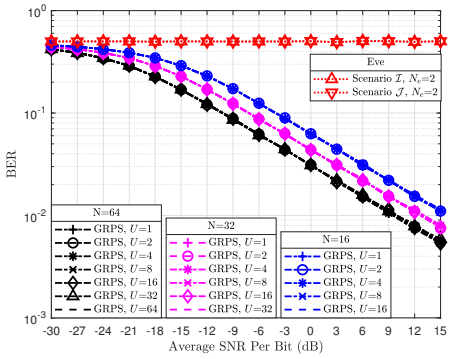

Fig. 6. Simulated BERs of Bob and Eve, when different N, U, and eavesdropping scenarios are considered for the IRS-USRSM with GRPS. $N_t = 1$, $N_b = 2$, $N_e = 2$ and $M = 4$.

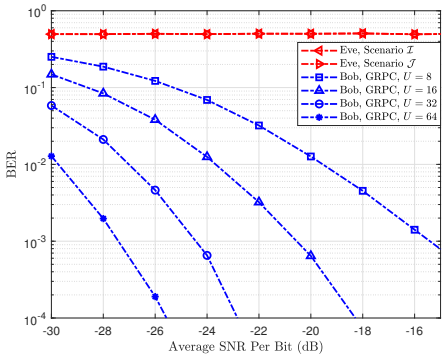

Fig. 7. Simulated BERs of Bob and Eve, when different U and eavesdropping scenarios are considered for the IRS-USRSM with GRPC. $N_t = 1$, $N_b = 2$, $N_e = 2$, $N = 64$, and $M = 4$.

is because, additional spatial diversity gain can be achieved as N increases, which can be utilized at Bob for achieving enhanced detection performance. However, given the same N, Bob's BER performance remains basically unchanged as U increases. This is in accordance with the prediction declared in Section III-A. Hence, given the RPS-kind schemes are exploited for practical applications, we only need to select the GRPS with single group ($U = 1$), which is capable of achieving the best possible transmission performance with the lowest implementation complexity.

In Fig. 7, we depict the simulated BER results of Bob and Eve for the GRPC based IRS-USRSM systems with different N, U, and eavesdropping scenarios. The number of IRS groups U is let to be increased from 8 to 16, 32, and then to 64, where the GRPC with $U = 64$ is actually the ERPC with $N = 64$. From Fig. 7, we can observe that the BER performance of Eve also remains around 0.5 in either scenario $\mathcal{I}$ or $\mathcal{J}$. Besides, the BER performance of Bob gradually improves as U increases. This is because by increasing U, the spatial diversity gain achieved by Bob can be improved for remarkable BER performance enhancement. In addition, given the same number of IRS elements N, the simulated EBR performance yielded by utilizing the GRPC with $U < 64$ can be worse than that by the ERPC. On the other hand, we can observe that as U increases, the simulated EBR result achieved by using the GRPC gradually approach that by the ERPC. This indicates that with the same group of IRS element share the common phase-shift for reflection, the GRPC is capable of assuring a certain level of BER performance with significantly decreases implementation complexity.

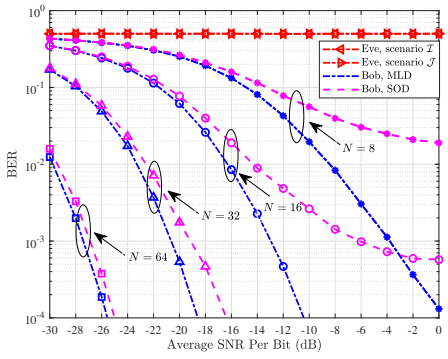

Fig. 8. Simulated BERs of IRS-USRSM systems with different detections at Bob and different eavesdropping scenarios at Eve. $N_t = 1$, $N_b = 2$, $N_e = 2$, $N \in \{8, 16, 32, 64\}$, and $M = 4$.

In Fig. 8, we show the simulated BER performance of Bob with different detection schemes and number of IRS reflecting elements N and that of Eve in different eavesdropping scenarios. Then the impacts of N on the performance discrepancy between Bob with MLD and SOD detections can be characterized apparently. From Fig. 8, we can depict the following observations. First, the simulated BER results of Eve are about 0.5 with negligible variations. Second, with the increase of SNR, the simulated BER results achieved by utilizing MLD and SOD at Bob decreases generally, the difference between them grows normally with the same N, while the BER performance achieved by the MLD always superior to that by the SOD. However, the BER performance discrepancy between Bob with MLD and SOD decreases dramatically as N increases. This is due to the fact that, with the increase of N, the detection of the receive antenna index at Bob becomes more dependable, thus improving the BER performance of the system while ensuring a lower detection complexity. These observations indicate that with a sufficient large N or at low SNR, the BER performance of the SOD approaches that of the MLD, while can be regarded as the BER performance upper limits for Bob with our proposal.

C. BER and ESR Comparisons of Different Uplink Transmissions

In Fig. 9, we draw and compare the simulated BER results of Eve with the proposed IRS-USRSM and the other three benchmark uplink SIMO transmission schemes, namely IRS-RSM, the conventional SIMO transmissions without IRS ('NoIRS') and with the random phase-shifts IRS ('Random'). For the conventional IRS-RSM, the BER performance of Eve is stably figured around 0.5 in scenario $\mathcal{J}$, but gradually improves with the increase of SNR also N_e in the scenario $\mathcal{I}$. Similarly, the NoIRS and Random schemes in each individual scenario are capable of achieving gradual degradations in BER as the SNR or N_e increases, which exemplifies poor transmission secrecy for the involved uplink SIMO systems. However, due to the injection of multiplicative transmitter perturbations, the BER results at Eve of the proposed IRS-USRSM system are always located around 0.5 for any of the

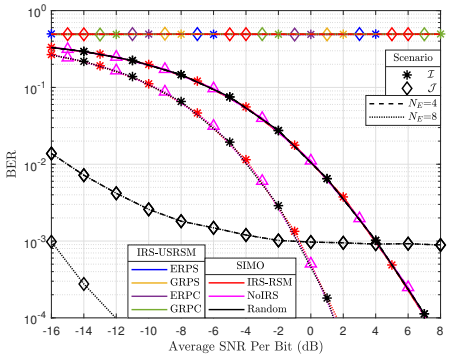

Fig. 9. Simulated BERs of Eve in different scenarios for the proposed and benchmark wiretapping systems. $N_t = 1$, $N_b = 2$, $N = 64$ and $M = 4$.

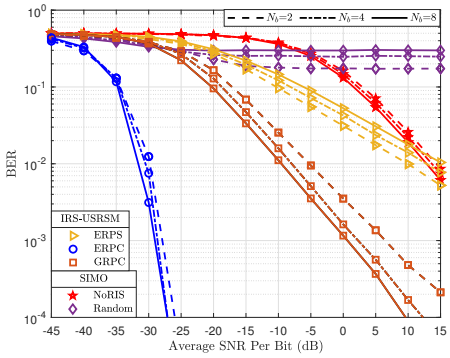

Fig. 10. Simulated BERs of Bob with different N_b for uplink SIMO systems assisted by different transmission schemes. $N_t = 1$, $N_b \in \{2, 4, 8\}$, $N = 64$, $U = 2$ and $M = 4$.

considered eavesdropping scenarios. Therefore, our proposed IRS-USRSM generally yields an undesirable interference effect on the signal detection at Eve, and thus is capable of realizing significantly enhanced security as "one-time pad" transmission in the physical layer.

In Fig. 10, we present and compare the BER results achieved at Bob with our proposed IRS-USRSM assisted SIMO and the other two benchmark uplink SIMO transmission schemes, namely the conventional SIMO transmissions without IRS ('NoIRS') and with the random phase-shifts IRS ('Random'). For each individual scheme, N_b is let to be increased from 2 to 4, and then to 8, so as to demonstrate the impact of N_b on the achieved error performance. As shown in Fig. 10, with the increase of SNR, the BER performance improves generally, except for that the SIMO transmission with random phase-shifts IRS achieves its performance floor at the high SNR region. Additionally, we can witness that the ERPC based IRS-USRSM is able to achieve the best error performance, then the GRPC and ERPS based IRS-USRSM, and the without IRS scheme, whilst the random phase-shifts IRS to have the worst BER performance. This highlights the importance of IRS in improving system BER performance and the efficiency of our proposed strategy in significantly improving the BER performance of the system. Moreover, at the low SNR region, the performance of the random phase-shifts IRS scheme is better than that of the without IRS scheme. On the contrary, at the high SNR region, the without IRS scheme outperforms the random phase-shifts IRS scheme. This is due to the fact that, with the increase of SNR, the spatial resolution at Bob degrades with the random IRS phase-shifts scheme, which leads to a decrease in the BER performance. Besides, the BER performance of the ERPC based IRS-USRSM, the GRPC based IRS-USRSM, and the without IRS based SIMO improves, while the BER performance of the ERPS based IRS-USRSM and the random phase-shifts IRS based SIMO degrades, as N_b increases.

In Fig. 11, we depict and compare the information transmission rates, information leakage rates, and ESR performance results achieved by the investigated uplink SIMO systems. Specifically, Fig. 11 (a), (b) and (c) characterize the simulated information transmission rates, information leakage rates, and ESRs achieved by the proposed ERPC and GRPC schemes with other benchmark schemes for scenarios $\mathcal{I}$ and $\mathcal{J}$ respectively. From Fig. 11, it can be seen that the proposed schemes achieve similar transmission and secrecy performance as the IRS-RSM, but much better performance than other benchmark schemes, even in the very low SNR region. Specifically, the investigated ERPC and GRPC schemes can be employed to achieve the highest transmission rate along with the lowest information leakage rate. This is due to the fact that based on the proposed scheme, Eve can eavesdrop the baseband information bits at most. Accordingly, the ESR demonstrates a first rise and then a fall to stabilize tendency. In addition, the ESR performance achieved in scenario $\mathcal{J}$ is observed to outperform that in scenario $\mathcal{I}$ in the low SNR region. The reason is that, the information leakage rate attained by Eve increases faster in scenario $\mathcal{I}$ than that in scenario $\mathcal{J}$. The above all illustrates that the proposal schemes can not only be utilized to attain a desirable BER performance for accomplishing reliable transmission, but also be capable of assisting significantly enhanced secure transmission.

D. Comparison of Simulated/Analytical BERs and DCMCCs

In Fig. 12, we display and compare the simulated BER and ABEP-UB results, theoretical ABEP-UB and ABEP-UPB results for the investigated IRS-USRSM. From Fig. 12, we can see that for a given system configuration, the best BER performance is obtained when $N = 64$. This is because, in this case, the receive antenna index can be detected more reliably than in other cases. In addition, we can observe that the theoretical results of ABEP-UB are more closely fitted with the numerical and simulated error performance results, while the theoretical ABEP-UPB results obtained by using the MGF method are getting to be tighter as an error performance upper-bound, as N increases. This validates the accuracy of derivations achieved in (28) and (34).

In Fig. 13, we depict the ESR and DCMCC performance results achieved by the investigated IRS-USRSM systems. Specifically, Fig. 13 (a) and (b) characterize the simulated and theoretical DCMCC and ESR results achieved by utilizing ERPC for scenarios $\mathcal{I}$ and $\mathcal{J}$ respectively. From Fig. 13, it can be seen that the simulated and theoretical ESR and DCMCC results fit generally well with each other for both scenarios $\mathcal{I}$ and $\mathcal{J}$. By contrast, Eve's theoretical DCMCC results provide an upper bound for its simulated results. Moreover, the

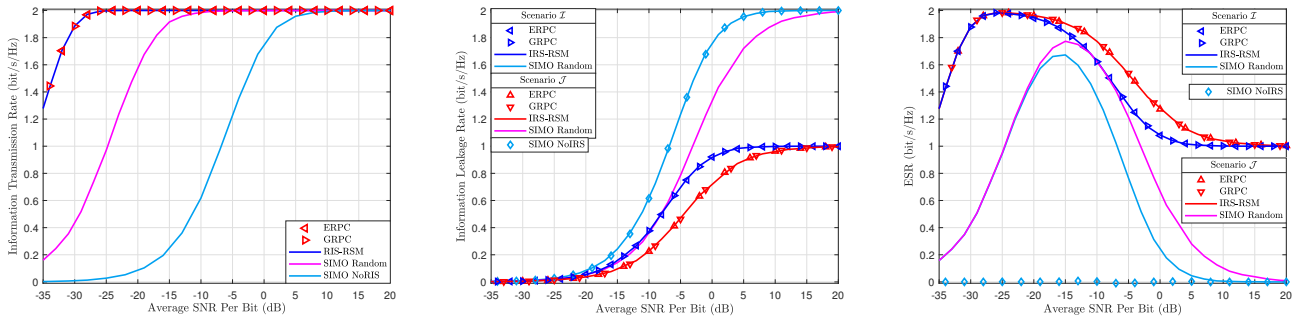

(a) (b) (c)

Fig. 11. Comparison of the simulated information transmission rates (a), information leakage rates (b), and ESRs (c) achieved by the investigated ERPC and GRPC schemes with other benchmark schemes. $N_t = 1$, $N_b = 2$, $N_e = 2$, $N = 64$, $U = 2$ and $M = 2$.

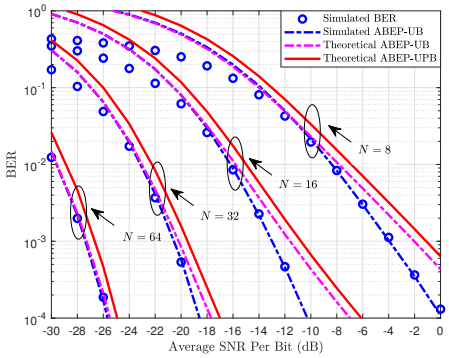

Fig. 12. Comparison of the simulated BER, ABEP-UB, and ABEP-UPB of Bob for the investigated IRS-USRSM. $N_t = 1$, $N_b = 2$, $N_e = 2$, $N \in \{8, 16, 32, 64\}$ and $M = 4$.

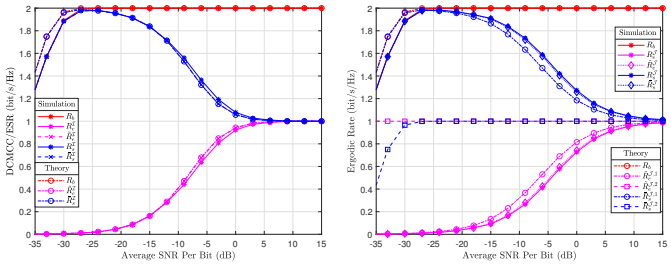

(a) (b)

Fig. 13. Comparison of the simulated and theoretical DCMCCs and ESRs achieved by the ERPC based IRS-USRSM systems with $\mathcal{I}$ (a) and scenario $\mathcal{J}$ (b), respectively. $N_t = 1$, $N_b = 2$, $N_e = 2$, $N = 64$, $U = 2$ and $M = 2$.

theoretical ESR and DCMCC results ($\bar{R}_s^{\mathcal{I}}$ and $\tilde{R}_e^{\mathcal{I}}$) derived for scenario $\mathcal{I}$ are observed to be much tighter to their simulated results than that for scenario $\mathcal{J}$ ($\bar{R}_s^{\mathcal{J}}$ and $\tilde{R}_e^{\mathcal{J},1}$). However, for scenario $\mathcal{J}$, the high-SNR Gamma approximation results ($\bar{R}_s^{\mathcal{J},2}$ and $\tilde{R}_e^{\mathcal{J},2}$), can only be accurate in the high SNR region. These in all substantiate the accuracy of our performance derivations of (68), (80) and (84)[2].

[2]Fig. 13 (a) depicts the performance results derived via mutual information analysis for Scenario $\mathcal{I}$. By contrast, Fig. 13 (b) characterizes the performance results achieved upon utilizing the per-SNR point and high SNR approximation based Gamma approximations for Scenario $\mathcal{J}$. Hence, although the two subfigures are illustrated in a similar manner, it is unnecessary to include high SNR approximation involved performance results in Fig. 13 (a).

VII. Conclusion

In this paper, we proposed and investigated a spatial modulation framework for uplink secure transmission. Based on this, IRS and secrecy signals were introduced into the framework in order to improve the security of the system. Then, based on the transmitter-side perturbation and IRS reflection, we proposed four different IRS reflection assisted JTPIR schemes, so as to achieve different levels of system performance and hardware complexity. In terms of signal detection, this paper proposed the MLD detection algorithm with optimal performance and the SOD detection algorithm with low computational complexity, respectively. Finally, closed-form system performance results of IRS-USRSM were evaluated upon rendering that the ERPC based JTPIR and the MLD detection is utilized. Finally, we compared the performance achieved by the proposed scheme with those of the benchmark schemes. Particularly, with the proposed JTPIR scheme being utilized, the BER at Eve always retains around 0.5, which is not assured with other benchmark schemes. Furthermore, assuming that Eve knows perfectly the CSI and perturbation information, the information leakage rate of the proposed scheme is nearly half to that with any of the traditional SIMO schemes. The resultant ESR of the proposed scheme is much larger than any of the other schemes, and can elevate to is limit at only about -25dB. Our studies in this paper demonstrate that, the IRS-USRSM system is capable of achieving high transmission efficiency and reliability, along with remarkably enhanced security.

VIII. Appendices

A. Proof of Theorem 1

According to definition, (67) can be rewritten as

$$R_b = \mathcal{H}(x_k) - \mathbb{E}_{\mathbf{G},\mathbf{h}}[\mathcal{H}(x_k; \mathbf{y}_b|\mathbf{G}, \mathbf{h}], \tag{73}$$

where, $\mathcal{H}(x_k) = -\sum_{x_k} p(x_k) \log p(x_k) = \log_2(M)$ is obtained due to independence of APM symbols, while the conditional entropy is simplified in (74) at the top of next page. Based on [40], we can have

$$p(\mathbf{y}_b|x_k = x_k, \mathbf{G}, \mathbf{h}) = \frac{1}{\pi\sigma_b} \exp\left(-\frac{\|\mathbf{y}_b - \mathbf{G}\mathbf{\Phi}_i \mathbf{h} w x_k\|^2}{{\sigma_b}^2}\right), \tag{75}$$

$$\mathcal{H}(x_k|\mathbf{y}_b,\mathbf{G},\mathbf{h}) = -\int p(x_k)\int p(\mathbf{y}_b,\mathbf{G},\mathbf{h}|x_k)\log p(\mathbf{y}_b,\mathbf{G},\mathbf{h}|x_k)d\mathbf{y}_b dx_k$$
$$= \frac{1}{M}\sum_{k=1}^{M}\int_{\mathbf{y}_b} p(\mathbf{y}_b|x_k=x_k,\mathbf{G},\mathbf{h})\log_2\frac{p(\mathbf{y}_b)}{\frac{1}{M}p(\mathbf{y}_b|x_k=x_k,\mathbf{G},\mathbf{h})}d\mathbf{y}_b. \quad (74)$$

$$p(\mathbf{y}_b) = \frac{1}{M}\frac{1}{\pi\sigma_b}\sum_{m'=1}^{M}\exp(-\frac{\|\mathbf{y}_b-\mathbf{G}\mathbf{\Phi}_i\mathbf{h}wx_{\hat{k}}\|^2}{{\sigma_b}^2}). \quad (76)$$

Upon substituting (74)-(76) into (73), R_b can be simplified as

$$R_b = \log_2(N_bM) - 1/(N_bM)\sum_{i,k}\mathbb{E}_{\mathbf{G},\mathbf{h},\mathbf{n}_b}[$$
$$\log_2\sum_{\hat{i},\hat{k}}\exp(\frac{-\|\mathbf{r}_{i,k}-\mathbf{r}_{\hat{i},\hat{k}}+\mathbf{n}_b\|^2+\|\mathbf{n}_b\|^2}{\sigma_b^2})]. \quad (77)$$

By applying the Jensen's inequality and the analyzing method in [41], we can achieve $\tilde{R}_b$ in (68) and complete the proof.

B. Proof of Theorem 2

Let Eve's signal observations of (5) and (6) be aggregately expressed as $\mathbf{y}_e = \mathbf{U}x_k + \mathbf{n}_e$, where $\mathbf{U}$ is the equivalent channel in general. Then, by following the derivations of VIII-A, we can simplify R_e as

$$R_e = \mathbb{E}_{\mathbf{U}}\{I(x_k;\mathbf{y}_e|\mathbf{U})\} = \mathcal{H}(x_k) - \mathbb{E}_{\mathbf{U}}[\mathcal{H}(x_k;\mathbf{y}_e|\mathbf{U})]$$
$$= \log_2 M - \frac{1}{M}\sum_{k=1}^{M}\mathbb{E}_{\mathbf{U},\mathbf{n}_e}[\log_2\sum_{k'=1}^{M}\exp(-\frac{\delta+\|\mathbf{n}_b\|^2}{{\sigma_e}^2})]$$
$$= \log_2 M - N_e/\ln 2 - \frac{1}{M}\sum_{k=1}^{M}\mathbb{E}_{\mathbf{U},\mathbf{n}_e}[\log_2\sum_{k'=1}^{M}\exp(-\frac{\delta}{{\sigma_e}^2})]. \quad (78)$$

where $\delta = ||\mathbf{U}(x_k - x_{\hat{k}}) + \mathbf{n}_e||^2$.

C. Proof of Theorem 3

For scenario $\mathcal{I}$, upon utilizing (5) and the derivations in (78), we derive $R_e^{\mathcal{I}}$ as (79) at the bottom of next page, where the equivalent channel is denoted as $\tilde{\mathbf{c}} = \mathbf{c}w$. Due to the convexity of $\log[\sum_m \exp(x_m)]$, the upper-bound of $R_e^{\mathcal{I}}$ can be obtained as (80), where equation a is derived by extracting the noise terms from (79), equation b is obtained on the basis that $||\tilde{\mathbf{c}}||^2$ satisfies the Gamma distribution of $\Gamma(N_e,1)$, equation c is achieved upon utilizing $(3.381,4)$ in [42].

By contrast, in scenario $\mathcal{J}$, the equivalent noise at Eve is expressed as $\tilde{\mathbf{n}}_e = \mathbf{F}\mathbf{\Phi}_i\mathbf{h}wx_k + \mathbf{n}_e$, which is colored Gaussian noise. The variance of the equivalent noise is conveyed as

$$\mathbf{\Sigma} = \mathbb{E}[\tilde{\mathbf{n}}_e(\tilde{\mathbf{n}}_e)^H] = \mathbf{F}\mathbf{\Phi}_i\mathbf{h}(\mathbf{F}\mathbf{\Phi}_i\mathbf{h})^H + \sigma_e^2\mathbf{I}, \quad (81)$$

By multiplying $\mathbf{y}_e^{\mathcal{J}}$ with $\mathbf{\Sigma}^{-1/2}$, we can obtain noise-whitening signal observation at Eve as $\mathbf{y}_w = \mathbf{\Sigma}^{-1/2}\mathbf{y}_e^{\mathcal{J}} = \mathbf{c}_w wx_k + \mathbf{n}_w$, where $\mathbf{c}_w = \mathbf{\Sigma}^{-1/2}\mathbf{c}$ and $\mathbf{n}_w = \mathbf{\Sigma}^{-1/2}\tilde{n}_e^m$. Then, we can have $\mathbf{y}_w \sim \mathcal{CN}(\alpha\mathbf{c}wx_k, \sigma_e^2\mathbf{I})$. Let $\tilde{\mathbf{c}}_w = \mathbf{c}_w w = \mathbf{\Sigma}^{-1/2}\tilde{\mathbf{c}}$ be the whitened equivalent channel. We can derive $R_e^{\mathcal{J}}$ as (82) and its upper bound $\tilde{R}_e^{\mathcal{J}}$ can be obtained by applying Jensen's inequality as (83). As the distribution of $\tilde{\mathbf{c}}_w$ is difficult to obtain, we consider two methods for approximate analysis. The first method is referred to as the per SNR point γ based Gamma approximation, by which the parameters of approximated Gamma distribution is achieved as ε_γ and β_γ [43]. The second method is the high SNR based Gamma approximation, where $\hat{\mathbf{c}}_w$ is approximated with an Gamma distribution by letting σ_e^2 approaches 0. Consequently, by following the procedures for deriving (80), the closed-form upper-bounds of (84) and (85) can be obtained.

REFERENCES

[1] F. Yu, Z. Shi, C. Liu, M. Lin, T.-X. Zheng, B. Liu, and G. Lu, "Secure uplink spatial modulation enabled by IRS," in *Proc. IEEE 98th Veh. Technol. Conf. (VTC2023-Fall)*, Hong Kong, Oct. 2023, pp. 1–6.

[2] H. Zhang, B. Li, M. Karimi, S. Saydam, and M. Hassan, "Recent advancements in IoT implementation for environmental, safety, and production monitoring in underground mines," *IEEE Internet Things J.*, vol. 10, no. 16, pp. 14 507–14 526, Aug. 2023.

[3] B. A. Salau, A. Rawal, and D. B. Rawat, "Recent advances in artificial intelligence for wireless Internet of Things and cyber–physical systems: A comprehensive survey," *IEEE Internet Things J.*, vol. 9, no. 15, pp. 12 916–12 930, Aug. 2022.

[4] H. Rahmani, D. Shetty, M. Wagih, Y. Ghasempour, V. Palazzi, N. B. Carvalho, R. Correia, A. Costanzo, D. Vital, F. Alimenti, J. Kettle, D. Masotti, P. Mezzanotte, L. Roselli, and J. Grosinger, "Next-generation IoT devices: Sustainable eco-friendly manufacturing, energy harvesting, and wireless connectivity," *IEEE J. Microw.*, vol. 3, no. 1, pp. 237–255, Jan. 2023.

[5] G. Moloudian, M. Hosseinifard, S. Kumar, R. B. V. B. Simorangkir, J. L. Buckley, C. Song, G. Fantoni, and B. O'Flynn, "RF energy harvesting techniques for battery-less wireless sensing, industry 4.0 and Internet of Things: A review," *IEEE Sens. J.*, 2024.

[6] M. Z. Siddiqi and T. Mir, "Reconfigurable intelligent surface-aided wireless communications: An overview," *Intell. Converged Netw.*, vol. 3, no. 1, pp. 33–63, Mar. 2022.

[7] M. Fu, W. Mei, and R. Zhang, "Multi-active/passive-IRS enabled wireless information and power transfer: Active IRS deployment and performance analysis," *IEEE Commun. Lett.*, vol. 27, no. 8, pp. 2217–2221, Jun. 2023.

[8] H. Wei and H. Zhang, "An equivalent model for handover probability analysis of IRS-aided networks," *IEEE Trans. Veh. Technol.*, vol. 72, no. 10, pp. 13 770–13 774, May 2023.

[9] M. Di Renzo, A. Zappone, M. Debbah, M.-S. Alouini, C. Yuen, J. de Rosny, and S. Tretyakov, "Smart radio environments empowered by reconfigurable intelligent surfaces: How it works, state of research, and the road ahead," *IEEE J. Sel. Areas Commun.*, vol. 38, no. 11, pp. 2450–2525, Nov. 2020.

[10] M. Jian, G. C. Alexandropoulos, E. Basar, C. Huang, R. Liu, Y. Liu, and C. Yuen, "Reconfigurable intelligent surfaces for wireless communications: Overview of hardware designs, channel models, and estimation techniques," *Intell. Converg. Netw.*, vol. 3, no. 1, pp. 1–32, Mar. 2022.

[11] R. Liang and J. Fan, "Energy-efficient mmwave IoT communications with multihop IRS-assisted systems," *IEEE Internet Things J.*, vol. 10, no. 21, pp. 19 344–19 355, Aug. 2023.

[12] K. Tekbıyık, G. K. Kurt, and H. Yanikomeroglu, "Energy-efficient RIS-assisted satellites for IoT networks," *IEEE Internet Things J.*, vol. 9, no. 16, pp. 14 891–14 899, Aug. 2022.

[13] Y. Zou, Y. Liu, X. Mu, X. Zhang, Y. Liu, and C. Yuen, "Machine learning in RIS-assisted NOMA IoT networks," *IEEE Internet Things J.*, vol. 10, no. 22, pp. 19 427–19 440, Nov. 2023.

[14] C. Liu, J. Ma, P. Zhai, B. Liu, T.-X. Zheng, and F. Wang, "Enabling joint transmitter-receiver spatial modulation with RF mirrors: A low-cost and highly-flexible perspective," *Digit. Signal Process.*, vol. 133, Mar. 2023.

$$R_e^{\mathcal{I}} = \log_2 M - N_e/\ln 2 - \frac{1}{M}\sum_{k=1}^{M}\mathbb{E}_{\tilde{\mathbf{c}},\mathbf{n}_e}[\log_2\sum_{k'=1}^{M}\exp(\frac{-||\tilde{\mathbf{c}}x_k - \tilde{\mathbf{c}}x_{\hat{k}} + \mathbf{n}_e||^2}{{\sigma_e}^2})] \tag{79}$$

$$\begin{aligned}\tilde{R}_e^{\mathcal{I}} &\overset{a}{=} \log_2 M + N_e - N_e/\ln 2 - \frac{1}{M}\sum_{k=1}^{M}\log_2\sum_{k'=1}^{M}\mathbb{E}_{\tilde{\mathbf{c}}}[\exp(-\frac{||\tilde{\mathbf{c}}||^2|x_k - x_{\hat{k}}|^2}{2{\sigma_e}^2})]\\ &\overset{b}{=} \log_2 M + N_e - N_e/\ln 2 - \frac{1}{M}\sum_{k=1}^{M}\log_2\sum_{k'=1}^{M}\int_0^{\infty}\exp(-\frac{t|x_k - x_{\hat{k}}|^2}{2{\sigma_e}^2})t^{N_e-1}\frac{\exp(-t)}{\Gamma(N_e)}dt\\ &\overset{c}{=} \log_2 M + N_e - N_e/\ln 2 - \frac{1}{M}\sum_{k=1}^{M}\log_2\sum_{k'=1}^{M}(1+\frac{|x_k - x_{\hat{k}}|^2}{2{\sigma_e}^2})^{-N_e}.\end{aligned} \tag{80}$$

$$R_e^{\mathcal{J}} = \log_2 M - N_e/\ln 2 - \frac{1}{M}\sum_{m=1}^{M}\mathbb{E}_{\tilde{\mathbf{c}}_w,\mathbf{n}_w}[\log_2\sum_{m'=1}^{M}\exp(-\|\tilde{\mathbf{c}}_w x_k - \tilde{\mathbf{c}}_w x_{\hat{k}} + \mathbf{n}_w\|^2)] \tag{82}$$

$$\tilde{R}_e^{\mathcal{J}} = \log_2 M + N_e - N_e/\ln 2 - \frac{1}{M}\sum_{k=1}^{M}\log_2\sum_{k'=1}^{M}\mathbb{E}_{\tilde{\mathbf{c}}_w}[\exp(\frac{-||\tilde{\mathbf{c}}_w||^2|x_k - x_{\hat{k}}|^2}{2})] \tag{83}$$

$$\begin{aligned}\tilde{R}_e^{\mathcal{J},1} &= \log_2 M + N_e - N_e/\ln 2 - \frac{1}{M}\sum_{k=1}^{M}\log_2\sum_{k'=1}^{M}\int_0^{\infty}\exp(\frac{-t|x_k - x_{\hat{k}}|^2}{2})t^{\varepsilon_\gamma-1}\beta_\gamma^{-\varepsilon_\gamma}\frac{\exp(-t/\beta_\gamma)}{\Gamma(\varepsilon_\gamma)}dt\\ &= \log_2 M + N_e - N_e/\ln 2 - \frac{1}{M}\sum_{k=1}^{M}\log_2\sum_{k'=1}^{M}(1+\frac{\beta_\gamma|x_k - x_{\hat{k}}|^2}{2})^{-\varepsilon_\gamma}\end{aligned} \tag{84}$$

$$\begin{aligned}\tilde{R}_e^{\mathcal{J},2} &= \log_2 M + N_e - N_e/\ln 2 - \frac{1}{M}\sum_{k=1}^{M}\log_2\sum_{k'=1}^{M}\mathbb{E}_{\hat{\mathbf{c}}_w}[\exp(\frac{-||\hat{\mathbf{c}}_w||^2|x_k - x_{\hat{k}}|^2}{2})]\\ &= \log_2 M + N_e - N_e/\ln 2 - \frac{1}{M}\sum_{k=1}^{M}\log_2\sum_{k'=1}^{M}(1+\frac{\hat{\beta}|x_k - x_{\hat{k}}|^2}{2})^{-\hat{\varepsilon}}\end{aligned} \tag{85}$$

[15] G. Zhang, X.-Q. Jiang, H. Hai, M. Wen, P. Shang, and S. Wei, "Joint code index modulation aided enhanced spatial modulation for high-rate MIMO systems," *IEEE Trans. Green Commun. Netw.*, vol. 7, no. 3, pp. 1383–1393, Sep. 2023.

[16] W. M. Jang, "Transmitter space shift keying with maximum-ratio combining and receiver spatial modulation with maximum-ratio transmission in downlink cellular systems," *IEEE Trans. Veh. Technol.*, vol. 72, no. 8, pp. 10 633–10 643, Aug. 2023.

[17] Y. Zhan and F. Huang, "Generalized spatial modulation with multi-index modulation," *IEEE Commun. Lett.*, vol. 24, no. 3, pp. 585–588, Mar. 2020.

[18] J. Ma, C. Liu, T.-X. Zheng, C. Liu, and G. Lu, "Augmented pattern index modulation empowered by RIS," in *Proc. IEEE Int. Conf. Commun. (ICC)*, Seoul, Korea, Republic of, May 2022, pp. 2858–2863.

[19] Q. Li, M. Wen, J. Li, Z. He, and Y. Yan, "Interplay between reconfigurable intelligent surfaces and spatial modulation: New application paradigms," *IEEE Wireless Commun.*, vol. 30, no. 1, pp. 126–133, Nov. 2023.

[20] B. A. Ozden, E. Aydin, and F. Cogen, "Reconfigurable intelligent surface-aided spatial media-based modulation," *IEEE Trans. Green Commun. Netw.*, vol. 7, no. 4, pp. 1971–1980, Dec. 2023.

[21] X. Bi, P. Shang, Y. Peng, K. Peng, and H. Hai, "Space-time block coded reconfigurable intelligent surfaces-based generalized spatial modulation," in *Proc. IEEE/CIC Int. Conf. Commun. China (ICCC)*, Foshan, China, Aug. 2022, pp. 350–354.

[22] K. S. Sanila and N. Rajamohan, "Intelligent reflecting surface assisted transceiver quadrature spatial modulation," *IEEE Commun. Lett.*, vol. 26, no. 7, pp. 1653–1657, Jul. 2022.

[23] M. Lin, C. Liu, Q. Wu, and W. Wang, "DF-relay-assisted multi-antenna D2D covert communication in the presence of joint detection," *IEEE Internet Things J.*, Nov. 2023.

[24] N. Wang, P. Wang, A. Alipour-Fanid, L. Jiao, and K. Zeng, "Physical-layer security of 5G wireless networks for IoT: Challenges and opportunities," *IEEE Internet Things J.*, vol. 6, no. 5, pp. 8169–8181, Oct. 2019.

[25] J. Li, P. Wang, L. Jiao, Z. Yan, K. Zeng, and Y. Yang, "Security analysis of triangle channel-based physical layer key generation in wireless backscatter communications," *IEEE Trans. Inf. Forensics Security*, vol. 18, pp. 948–964, Nov. 2023.

[26] S. E. Zegrar, H. M. Furqan, and H. Arslan, "Flexible physical layer security for joint data and pilots in future wireless networks," *IEEE Trans. Commun.*, vol. 70, no. 4, pp. 2635–2647, Apr. 2022.

[27] M. Mitev, A. Chorti, H. V. Poor, and G. P. Fettweis, "What physical layer security can do for 6G security," *IEEE Open J. Veh. Technol.*, vol. 4, pp. 375–388, Feb. 2023.

[28] P. Yang, X. Qiu, and F. Mu, "Artificial noise-aided secure generalized spatial modulation for multiuser transmission," *IEEE Commun. Lett.*, vol. 24, Nov. 2020.

[29] W. Yin, Z. Kong, Y. Liu, Y. Yang, and L. Hanzo, "Artificial-noise-aided CQI-mapped generalized spatial modulation," *IEEE Trans. Veh. Technol.*, vol. 72, no. 4, Apr. 2023.

[30] J. Jian, W.-Q. Wang, A. Basit, and B. Huang, "Physical layer security for frequency diverse array-based dual-hop spatial modulation," *IEEE Trans. Wireless Commun.*, vol. 22, Nov. 2023.

[31] F. Shu, L. Yang, X. Jiang, W. Cai, W. Shi, M. Huang, J. Wang, and X. You, "Beamforming and transmit power design for intelligent

reconfigurable surface-aided secure spatial modulation," *IEEE J. Sel. Topics Signal Process.*, vol. 16, no. 5, pp. 933–949, Aug. 2022.
[32] E. Panayirci, M. Koca, H. Haas, and H. V. Poor, "Spatial modulation aided physical layer security for NOMA-VLC systems," *IEEE Trans. Veh. Technol.*, vol. 72, Aug. 2023.
[33] S. Arzykulov, A. Celik, G. Nauryzbayev, and A. M. Eltawil, "Artificial noise and RIS-aided physical layer security: Optimal RIS partitioning and power control," *IEEE Wireless Commun. Lett.*, vol. 12, no. 6, pp. 992–996, Jun. 2023.
[34] Y. Zhang, S. Zhao, Y. Shen, X. Jiang, and N. Shiratori, "Enhancing the physical layer security of two-way relay systems with RIS and beamforming," *IEEE Trans. Inf. Forensics Security*, vol. 19, pp. 5696–5711, May 2024.
[35] S. Cai, H. Qu, J. Zhang, X. Shi, and H. Zhu, "Symbol-level precoding design in IRS-aided secure wireless communication systems," *IEEE Wireless Commun. Lett.*, vol. 11, no. 11, pp. 2315–2319, Nov. 2022.
[36] E. Basar, "Reconfigurable intelligent surface-based index modulation: A new beyond MIMO paradigm for 6G," *IEEE Trans. Commun.*, vol. 68, no. 5, pp. 3187–3196, May 2020.
[37] M. Simon and M. Alouini, *Digital communication over fading channels*. New York: John Wiley & Sons, 2005.
[38] T. Ma, Y. Xiao, X. Lei, P. Yang, X. Lei, and O. A. Dobre, "Large intelligent surface assisted wireless communications with spatial modulation and antenna selection," *IEEE J. Sel. Areas Commun.*, vol. 38, no. 11, pp. 2562–2574, Nov. 2020.
[39] M. Chiani, D. Dardari, and M. Simon, "New exponential bounds and approximations for the computation of error probability in fading channels," *IEEE Trans. Wireless Commun.*, vol. 2, no. 4, pp. 840–845, Jul. 2003.
[40] S. Lin, B. Zheng, G. C. Alexandropoulos, M. Wen, M. D. Renzo, and F. Chen, "Reconfigurable intelligent surfaces with reflection pattern modulation: Beamforming design and performance analysis," *IEEE Trans. Wireless Commun.*, vol. 20, no. 2, pp. 741–754, Feb. 2021.
[41] C. Liu, L.-L. Yang, and W. Wang, "Secure spatial modulation with a full-duplex receiver," *IEEE Wireless Commun. Lett.*, vol. 6, no. 6, pp. 838–841, Dec. 2017.
[42] I. Gradshteyn and I. Ryzhik, *Table of integrals, series and products, 7th ed.* San Diego, CA, USA: Academic, 2007.
[43] P. J. Smith, R. Senanayake, and P. A. Dmochowski, "How accurate is your Gaussian/Gamma approximation?" *IEEE Wireless Commun. Lett.*, vol. 7, no. 5, pp. 804–807, Oct. 2018.

Chaowen Liu (Member, IEEE) received the B.S. degree in electrical engineering from Henan University of Science and Technology, Luoyang, China, in 2011, and the Ph.D. degree in information and communication engineering from Xi'an Jiaotong University, Xi'an, China, in 2018. From 2015 to 2017, he has been a Visiting Ph.D. Student with the School of Electronics and Computer Science, University of Southampton, UK. He is currently a Lecturer with Xi'an University of Posts and Telecommunications. His research interests include spatial-domain index modulation, physical-layer information security, full-duplex and metasurface aided wireless, and covert communications.

Zhengmin Shi (Graduate Student Member, IEEE) received the B.S. degree in 2022 from the Xi'an University of Posts and Telecommunications, Xi'an, China, where he is currently working toward the M.S. degree in electronic and information engineering. His research interests are spatial modulation, intelligent reflecting surface, and physical layer security.

Menghan Lin (Graduate Student Member, IEEE) received the B.E. degree in information engineering from Xi'an Jiaotong University, Xi'an, China, in 2018, where he is currently pursuing the Ph.D. degree in information and communication engineering. His research interests include covert communication and source location privacy.

Fei Yu (Graduate Student Member, IEEE) received the B.S. degree in Luoyang Normal University, Luoyang, China, in 2021. He is currently working toward the M.S. degree in Xi'an University of Posts and Telecommunications, Xi'an, China. His research interests are in the area of the physical layer security, intelligent reflecting surface, and covert communications.

Tong-Xing Zheng (Member, IEEE) received the B.S. degree in information engineering and the Ph.D. degree in information and communications engineering from Xi'an Jiaotong University, Xi'an, China, in 2010 and 2016, respectively. From 2017 to 2018, he was a Visiting Scholar with the School of Electrical Engineering and Telecommunications, The University of New South Wales, Sydney, Australia. He is currently an Associate Professor with Xi'an Jiaotong University. He has coauthored the book Physical Layer Security in Random Cellular Networks (Springer, 2016) and one book chapter. He has authored or coauthored over 70 papers in telecommunications journals and conference proceedings. His current research interests include 5G and 6G wireless networks and key technologies, physical layer security, and covert communications. He was a recipient of the Excellent Doctoral Dissertation Award of Shaanxi Province in 2019 and the First Prize of Science and Technology Award in Higher Institution of Shaanxi Province in 2019. He was honored as an Exemplary Reviewer of IEEE TRANSACTIONS ON COMMUNICATIONS in 2017, 2018, and 2021. He was a Leading Guest Editor of the Special Issue on Covert Communications for Next-Generation Wireless Networks of Frontiers in Communications and Networks in 2021 and a Guest Editor of the Special Issue on Physical Layer Security for Internet of Things of Wireless Communications and Mobile Computing in 2018. He is currently serving as an Associate Editor for IET Electronics Letters and a Review Editor for Frontiers in Communications and Networks.

Jiankang Zhang (Senior Member, IEEE) is a Senior Lecturer at Bournemouth University. Prior to joining in Bournemouth University, he was a senior research fellow at University of Southampton, UK. Dr Zhang was a lecturer from 2012 to 2013 and then an associate professor from 2013 to 2014 at Zhengzhou University. His research interests are in the areas of aeronautical communications and networks, evolutionary algorithms, machine learning algorithms and edge computing. He serves as an Associate Editor for IEEE ACCESS.

Guangyue Lu (Member, IEEE) received the Ph.D. degree from Xidian University, Xi'an, China, in 1999. From September 2004 to August 2006, he was a Guest Researcher with the Signal and Systems Group, Uppsala University, Uppsala, Sweden. Since 2005, he has been a Full Professor with the School of Communications and Information Engineering, Xi'an University of Posts and Telecommunications, Xi'an. He has been funded by over twenty projects including the National Natural Science Foundation of China, the 863 Program, and Important National Science and Technology Specific Projects. Due to his excellent contributions in education and research, he was awarded by the Program for New Century Excellent Talents in University, Ministry of Education, P. R. China, in 2009. His research interests include wireless communications, energy harvesting, cognitive radio and cooperative spectrum sensing. Currently, he is the Vice President of Xi'an University of Posts and Telecommunications, and the Director of the Shaanxi Key Laboratory of Information Communication Network and Security.